NEO Encounter 2029

Orbital Prediction via Differential Algebra and Taylor Models

Final Report

Authors: F. Bernelli-Zazzera, M. Lavagna, R. Armellin, P. Di Lizia, F. Topputo
Affiliation: Aerospace Engineering Department, Politecnico di Milano

Authors: M. Berz, K. Makino, R. Jagasia
Affiliation: Department of Physics and Astronomy, Michigan State University

ESA Researcher(s): Dario Izzo

Date: March 2009

Contacts:

Franco Bernelli-Zazzera
Tel: +39 02 2399 8328
Fax: +39 02 2399 8334
e-mail: franco.bernelli@polimi.it

Advanced Concepts Team
Fax: +31(0)715658018
e-mail: act@esa.int

Available on the ACT website
http://www.esa.int/act

Ariadna ID: AO/1-5680/08/NL/CB
Study Duration: 4 months
Contract Number: 20271/06/NL/HI

Contents

List of Figures

List of Tables

Abstract

The application of differential algebra and Taylor models to the analysis and prediction of Apophis close encounter is presented. The high order expansion of the flow of ordinary differential equations obtained by differential algebra is exploited to develop tools for the prediction of planetary encounters and potential impacts, taking into account the uncertainties due to measurement accuracy. A computationally efficient Monte Carlo simulation, an algorithm for the computation of the minimum distance between Earth and all the virtual asteroids belonging to the initial uncertainty cloud, and an impact leading algorithm capable of computing the initial conditions leading to an Earth impact are presented. Furthermore, a set of tools based on resonant distance minimization and resonant period constraint are enabled by differential algebra. Taylor model integrators are used to rigorously integrate all the possible Apophis initial conditions expressed as interval boxes. It is shown that the Taylor model based integration outperforms the validated integration tools based on interval arithmetic and that long-term integrations of the heliocentric phase can be addressed. Furthermore, an automatic box splitting algorithm and a particular attention with the coding of the dynamical system enable the validated integration of Apophis close encounter phase, which is a particularly challenging problem due to the high nonlinearities of the dynamics.

Key words: Differential Algebra, Taylor Model, Apophis Close Encounter, Impact Leading Conditions, Uncertainty Propagation, Validated Integration, Resonant Return.

Chapter 1

Introduction

Recently, several tools and techniques have been developed for the robust detection and prediction of planetary encounters and potential impacts by near-Earth asteroids [1, 2, 3]. However, these methods are neither sufficiently accurate when relying on simplifications (e.g., linear approximations) nor computationally efficient when based on several integration runs (e.g., in Monte Carlo approach).

Differential algebraic (DA) techniques [4] are proposed as a valuable tool to develop alternative approaches to tackle the previous tasks. Differential algebra provides the tools to compute the derivatives of functions within a computer environment. More specifically, by substituting the classical implementation of real algebra with the implementation of a new algebra of Taylor polynomials, any function f of v variables is expanded into its Taylor series up to an arbitrary order n. This has an important consequence when the numerical integration of an ordinary differential equation (ODE) is performed by means of an arbitrary integration scheme. Any explicit integration scheme is based on algebraic operations, involving the evaluations of the ODE right hand side at several integration points. Therefore, carrying out all the evaluations in the DA framework allows differential algebra to compute the arbitrary order expansion of the flow of a general ODE initial value problem.

The availability of such high order expansions is exploited to develop tools for the prediction of planetary encounters and potential impacts taking into account measurement uncertainties. More specifically, an improvement of Monte Carlo simulation approach is first obtained by replacing thousands integrations with evaluations of the high order expansion of the flow, reducing significantly the computational time and causing negligible loss in accuracy. The availability of high order maps in space and time and intrinsic tools for their inversion are then exploited in an algorithm that reduces the computa-

tion of the minimum distance from Earth and the corresponding epoch for all asteroids belonging to the initial uncertainties cloud to the simple evaluation of polynomials. Finally, an impact leading algorithm is developed to determine the initial conditions that would lead to an Earth's impact at any arbitrary observation epoch. Apophis asteroid is used as test case for all these algorithms.

Two DA-based tools for the analysis of Apophis close encounter in 2036 are implemented too. The first one is based on an ad hoc representation of Apophis' exit conditions from the encounter in 2029 and on the minimization of the Taylor map representing the asteroid's distance from the Earth at the resonant return. In the second one the asteroid 's orbital period after the first encounter is constrained to the one required for a 7:6 return. The compatibility of the achieved solutions with the set of Apophis initial conditions is checked too.

The second approach analyzed in the report concerns the use of Taylor models (TM) [5]. Taylor model integrators have recently shown to be a powerful tool for the validated integration of ordinary differential equations. By representing the flow of a differential equation by Taylor models, a tight enclosure for the action of the differential equations on an extended region for a time step Δt is then provided. Consequently, the integrated initial conditions can be either point vectors expressed by real numbers or interval boxes. Thus, either point or interval initial conditions can be rigorously integrated, allowing the propagation of uncertainty boxes on initial conditions. In this work the previous feature is exploited to rigorously predict the long-term motion of Near Earth Objects and the verified identification of impact occurrence.

These techniques are applied to dynamical models with a limited number of gravitational bodies and simplified ephemerides up to a n-body dynamics including also relevant non-gravitational perturbations and highly accurate ephemerides. In such a way the validated integration of the motion of a Near Earth Object (NEO) can be addressed considering initial uncertainties consistent with the current measurement accuracies. Again, Apophis asteroid is used as a test case. It is shown that Taylor model based integration outperforms classical interval schemes and that long-term verified integrations of the heliocentric phase can be easily addressed. Due to the high nonlinearity of the dynamics, the close encounter phase requires extra care. In particular, the dynamical model must be written in a suitable manner for Taylor model evaluation in order to avoid numerical inflation of the remainder bound. For this reason, simplified versions of the dynamics are developed and new features such as automatic box splitting are introduced in the validated integrator.

The report is organized as follows. The first chapter gives an overview on both DA and TM techniques. Particular attention is paid to the computation of n-th order expansion of the flow of ODE and on validated integration. In the second chapter all the models developed for the description of the dynamics and for the ephemeris functions are presented. Chapters 4 and 5 describe the algorithms and the results achieved both in the DA and TM frameworks. Final considerations on the work performed within the contract conclude the report.

Chapter 2

Notes on Differential Algebra and Taylor Models

In this chapter the tools used to perform the analysis are presented. Some notes on the theory of differential algebra and Taylor models are given together with their application to the integration of systems of ODE.

2.1 Notes on Differential Algebra

DA techniques find their origin in the attempt to solve analytical problems by an algebraic approach [4]. Historically, the treatment of functions in numerics has been based on the treatment of numbers, and the classical numerical algorithms are based on the mere evaluation of functions at specific points. DA techniques rely on the observation that it is possible to extract more information on a function rather than its mere values. The basic idea is to bring the treatment of functions and the operations on them to the computer environment in a similar way as the treatment of real numbers. Referring to Fig. 2.1, consider two real numbers a and b. Their transformation into the floating point representation, $\overline{a}$ and $\overline{b}$ respectively, is performed to operate on them in a computer environment. Then, given any operation $\times$ in the set of real numbers, an adjoint operation $\otimes$ is defined in the set of floating point (FP) numbers such that the diagram in Figure commutes[1]. Consequently, transforming the real numbers a and b into their FP representation and operating on them in the set of FP numbers return the same result as carrying out the operation in the set of real numbers and then transforming the achieved result in its FP representation. In a similar way, suppose two sufficiently regular functions f and g are given. In the framework of differential algebra,

[1]The diagram commutes approximately in practice, due to truncation errors.

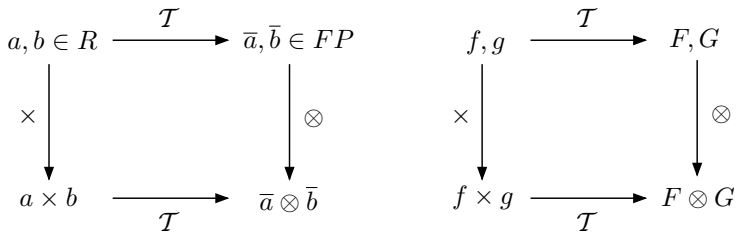

Figure 2.1: Analogy between the floating point representation of real numbers in a computer environment (left figure) and the introduction of the algebra of Taylor polynomials in the differential algebraic framework (right figure).

the computer operates on them using their Taylor series expansions, F and G respectively. Therefore, the transformation of real numbers in their FP representation is now substituted by the extraction of the Taylor expansions of f and g. For each operation in the space of sufficiently continuous functions, an adjoint operation in the space of Taylor polynomials is defined such that the corresponding diagram commutes; i.e., extracting the Taylor expansions of f and g and operating on them in the function space returns the same result as operating on f and g in the original space and then extracting the Taylor expansion of the resulting function. The straightforward implementation of differential algebra in a computer allows to compute the Taylor coefficients of a function up to a specified order n, along with the function evaluation, with a fixed amount of effort. The Taylor coefficients of order n for sums and product of functions, as well as scalar products with reals, can be computed from those of summands and factors; therefore, the set of equivalence classes of functions can be endowed with well-defined operations, leading to the so-called truncated power series algebra [6, 7].

Similarly to the algorithms for floating point arithmetic, the algorithm for functions followed, including methods to perform composition of functions, to invert them, to solve nonlinear systems explicitly, and to treat common elementary functions [8, 4]. In addition to these algebraic operations, also the analytic operations of differentiation and integration are introduced, so finalizing the definition of the DA structure. The differential algebra sketched in this section was implemented by M. Berz and K. Makino in the software COSY-Infinity [9].

2.2 High Order Expansion of the Flow

The differential algebra introduced in the previous section allows the derivatives of any function f of v variables to be computed up to an arbitrary order n, along with the function evaluation. This has an important consequence when the numerical integration of an ODE is performed by means of an arbitrary integration scheme. Any explicit integration scheme is based on algebraic operations, involving the evaluations of the ODE right hand side at several integration points. Therefore, carrying out all the evaluations in the DA framework allows differential algebra to compute the arbitrary order expansion of the flow of a general ODE initial value problem.

Without loss of generality, consider the scalar initial value problem

$$\begin{cases} \dot{x} = f(x,t) \\ x(t_i) = x_i. \end{cases} \tag{2.1}$$

Replace the point initial condition x_i by the DA representative of its identity function, $[x_i] = x_i^0 + \delta x_i$, where x_i^0 is the reference point for the expansion. If all the operations of the numerical integration scheme are carried out in the framework of differential algebra, the Taylor expansion of the solution with respect to the initial condition is obtained at each step. As an example, consider the forward Euler's scheme

$$x_k = x_{k-1} + \Delta t \cdot f(x_{k-1}) \tag{2.2}$$

and analyze the first integration step, i.e.,

$$x_1 = x_0 + \Delta t \cdot f(x_0), \tag{2.3}$$

where $x_0 = x_i$. Substitute the initial value with $[x_0] = [x_i] = x_i^0 + \delta x_i$ in (2.3) for

$$[x_1] = [x_0] + \Delta t \cdot f([x_0]). \tag{2.4}$$

If the function f is evaluated in the DA framework, the output of the first step, $[x_1]$, is the Taylor expansion of the solution x_1 at t_1 with respect to the initial condition about the reference point x_i^0. The previous procedure can be inferred through the subsequent steps until the last integration step is reached. At the final step the result is the n-th order Taylor expansion of the flow of the initial value problem (2.1) at the final time t_f. Thus, the expansion of the flow of a dynamical system can be computed up to order n with fixed amount of effort.

The previous DA-based numerical integrators pave the way to numerous practical applications, some of them being addressed in the remaining of this

work. A first example is presented hereafter pertaining to the propagation of errors on initial conditions. The Taylor polynomials resulting from the use of DA-based numerical integrators expand the solution of the initial value problem (2.1) with respect to the initial condition. Thus, at each integration step, the dependence of the solution x_k on the value of the initial condition x_i is available in terms of a polynomial map $\mathcal{M}_{x_k}(\delta x_i)$, where δx_i is the displacement of the initial condition x_i from the reference value x_i^0. Suppose now the reference value x_i^0 represents a nominal initial condition for a dynamical system, and assume some error δx_i occurs between the actual initial condition x_i and the nominal one. The evaluation of the Taylor polynomial $\mathcal{M}_{x_k}(\delta x_i)$ readily supplies the new solution x_k at time t_k corresponding to the displaced initial condition. More precisely, the Taylor polynomial $\mathcal{M}_{x_k}(\delta x_i)$ delivers a Taylor approximation of the new solution x_k, whose accuracy depends on the expansion order n and the size of the displacement δx_i. The main advantage of the DA-based integrator is that the new solution is obtained by means of the evaluation of a polynomial, so avoiding a new numerical integration corresponding to the displaced initial condition. Moreover, the same Taylor polynomial can be used to identify the solution corresponding to any error δx_i. Consequently, if many values of δx_i are to be processed, multiple simple polynomial evaluations can be efficiently performed in place of multiple intensive numerical integrations.

The results of the application of the previous procedure are illustrated in the following example. The dynamics of an object moving in the Solar System is integrated in the framework of the two body problem:

$$\begin{cases} \dot{\boldsymbol{r}} &= \boldsymbol{v} \\ \dot{\boldsymbol{v}} &= -\frac{\mu}{r^3}\,\boldsymbol{r}, \end{cases} \tag{2.5}$$

where $\boldsymbol{r}$ and $\boldsymbol{v}$ are the object position and velocity respectively, and μ is the Sun gravitational parameter. The nominal initial conditions are set such that the object starts moving from the pericenter of an elliptic orbit, lying on the ecliptic plane (see the dotted line in Fig. 2.2a). The pericenter radius is 1 AU, whereas the magnitude of the initial velocity is selected to have a resulting orbit of eccentricity 0.5. A DA-based 8-th order Runge–Kutta–Fehlberg (RKF78) scheme is used to expand the solution of the ODE (2.5) along one revolution of the resulting orbit. A box of initial positions 0.01 AU on each side is considered and its evolution is investigated. Given the bijectivity of the flow of (2.5), the boundary points of the initial uncertainty box propagate into boundary points of the corresponding solution set at each integration time. Consequently, the evolution of the initial box is studied by evolving its boundary. Based on the previous observation, a uniform

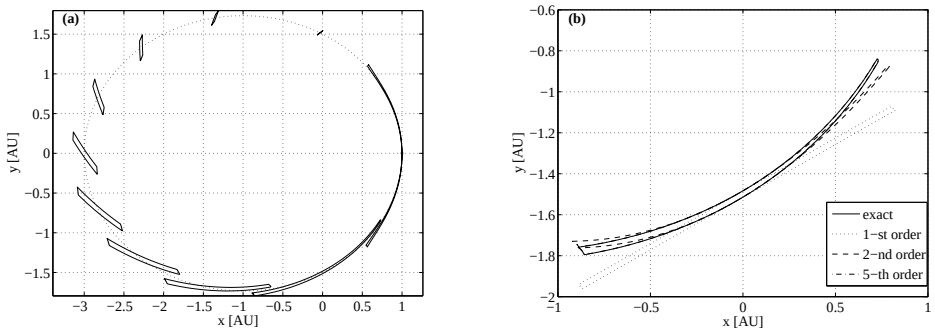

Figure 2.2: (**a**) Propagation of a box of initial positions in the two-body problem using the 5-th order expansion of the flow of the associated ODE; (**b**) accuracy analysis on one of the resulting boxes.

sampling of the boundary of the initial box is performed; for each sample, the displacement with respect to the nominal initial conditions is computed and the polynomial maps obtained by means of the DA-based integrator are evaluated. In this way, for each integration time, the evolved box can be readily plotted by means of mere polynomial evaluations. The evolved box is reported in Fig. 2.2a corresponding to 10 integration times uniformly distributed over the orbital period, using a 5-th order expansion of the flow of the ODE in (2.5). The time required by COSY-Infinity for the computation of the 5-th order map is about 0.38 s on a 2 GHz Intel Core Duo MacBook running Mac OS X.

The accuracy of the Taylor expansion of the flow is better highlighted in Fig. 2.2b. Focusing on a particular integration time, the exact propagated box is reported (solid line), which is based on a multiple point-wise integration of the samples. The propagated boxes obtained by the evaluation of the polynomial maps representing the flow of the ODE in (2.5) are then plotted for comparison, corresponding to different expansion orders. The figure shows that an accurate representation of the flow is already achieved using a 5-th order expansion of the flow.

2.3 Notes on Taylor Models

In the following, we give some notes on the Taylor model approach [10, 5] that will be used for the rigorous analysis of Apophis' close encounter. In particular we focus on verified ODE integration.

While interval-based methods can provide verification, it is commonly known that the overestimation due to the cancellation problem sometimes

limits their application for practical problems. To solve a system of multidimensional ordinary differential equations

$$\dot{\boldsymbol{r}} = \boldsymbol{f}(\boldsymbol{r}(t), t) \tag{2.6}$$

over long time with verification, the so-called wrapping effect adds a further difficulty. This effect is caused by the inflation of the size of the geometric set at each time step containing the validated solution set. Details about interval methods can be found in [11, 12, 13, 14, 15] as well as many other sources.

We propose the Taylor model approach, which combines high-order multivariate polynomial techniques and the interval technique for verification. Any $(n+1)$ times continuously partially differentiable function f in a domain D can be expressed by its n-th order Taylor polynomial $P_{n,f}$ at the expansion point $\boldsymbol{x}_0 \in D$, and a remainder bounded by an interval $I_{n,f}$ via

$$\forall \boldsymbol{x} \in D, \quad f(\boldsymbol{x}) \in P_{n,f}(\boldsymbol{x} - \boldsymbol{x}_0) + I_{n,f}. \tag{2.7}$$

From Taylor's theorem, the width of the remainder interval $I_{n,f}$ can be chosen to scale with the domain size proportional to $|\boldsymbol{x}-\boldsymbol{x}_0|^{n+1}$. By choosing the size $|\boldsymbol{x}-\boldsymbol{x}_0|$ small and the order n sufficiently high, the size of the remainder interval $I_{n,f}$ can be kept very small in practice. The bulk of the functional dependency is kept in the polynomial part $P_{n,f}$ with point coefficients, and there is no interval arithmetic associated inflation that happens in the polynomial part. Thus, the interval related overestimation is rather optimally suppressed with the Taylor model method [16]. The implementation of the method in the code COSY Infinity [5, 9] supports binary operations and standard intrinsic functions, as well as the antiderivative operation which widens the applications of the method.

The Taylor model based algorithm for a verified ODE integrator carries the functional dependency of the solutions on the initial conditions in the Taylor polynomial part. Thus it can optimally eliminate the wrapping effect, making possible not only to integrate over long time but also to deal with much larger domains of initial conditions.

A pair $(P_{n,f}, I_{n,f})$ satisfying (2.7) is called a Taylor model of f and denoted by

$$T_{n,f} = (P_{n,f}, I_{n,f}). \tag{2.8}$$

Taylor models of complicated functions f can be determined by carrying Taylor model arithmetic through binary operations and intrinsic functions

which compose the function f sequentially. Suppose we have Taylor models for g and h as $T_{n,g} = (P_{n,g}, I_{n,g})$ and $T_{n,h} = (P_{n,h}, I_{n,h})$. Then Taylor models of the sum and difference of g and h can be obtained as

$$T_{n,g} \pm T_{n,h} = (P_{n,g} \pm P_{n,h}, I_{n,g} \pm I_{n,h}). \tag{2.9}$$

The Taylor model for the product of g and h can be obtained as

$$T_{n,g} \cdot T_{n,h} = (P_{n,g\cdot h}, I_{n,g\cdot h}), \tag{2.10}$$

where $P_{n,g} \cdot P_{n,h} = P_{n,g\cdot h} + P_e$ with $P_{n,g\cdot h}$ being the n-th order polynomial of the result of the left hand side, and P_e the part of the product polynomial with order from $n+1$ to $2n$, and

$$I_{n,g\cdot h} = B(P_e) + B(P_{n,g}) \cdot I_{n,h} + B(P_{n,h}) \cdot I_{n,g} + I_{n,g} \cdot I_{n,h}, \tag{2.11}$$

where B denotes the bounds of the argument over the domain D. Refer to [10, 5] for the details on intrinsic functions including a multiplicative inverse of Taylor models.

The other important operation is the antiderivation operation, which is naturally available as an intrinsic function on the space of Taylor models. It has the form

$$\partial_i^{-1}(P_{n,f}, I_{n,f}) = \left(\int P_{n-1,f} dx_i \,,\ I_{n,\partial_i^{-1} f} \right), \tag{2.12}$$

where $I_{n,\partial_i^{-1} f} = (B(P_{n,f} - P_{n-1,f}) + I_{n,f}) \cdot B(x_i)$.

2.4 Validated Integration of ODE

In this section we review the key elements of the verified integration of ODE through Taylor models (for details refer to [5, 17]) and we present the main features of the new validated integrator [20]. Compared to other verified ODE integrators, both of the integrators used within this contract have the following characteristics:

- Because the solution set is described as a Taylor model describing the dependence on initial conditions, in subsequent operations the dependency problem based on the repeated use of the solution set, which is the source of the wrapping effect, can be avoided.
- For nonlinear ODE, the sharpness of the inclusion of the true solution set for each time step scales with order $(n+1)$ in the original domain width, and not order 2 as in the case of inclusion in interval boxes, polygons, or zonotopes used by other approaches. This allows larger domains to be transported without significant overestimation.

- The method naturally combines both first inclusion, commonly known as Algorithm I, as well as verification inclusion, commonly known as Algorithm II, into one high-order step.

- Because of the use of the intrinsic antiderivation operation, there is no need for explicit use of any error bounding formulas based on higher derivatives; rather, the error verification happens automatically as part of the integration step.

2.4.1 Old Validated Integration Tool

Flow Operator

The algorithm consists of the following basic steps. First, as it is commonly done, we re-write the ODE (2.6) in the form of an integral equation

$$\boldsymbol{r}(t) = \boldsymbol{r}_0 + \int_{t_0}^{t} \boldsymbol{f}(\boldsymbol{r}(t'), t')\, dt', \tag{2.13}$$

and with the introduction of the operator on the space of continuous functions from $[t_0, t_1]$ to R^v given by $A(\boldsymbol{\phi})(t) = \boldsymbol{r}_0 + \int_{t_0}^{t} \boldsymbol{f}(\boldsymbol{\phi}(t'), t')\, dt'$, we arrive at a fixed point problem $\boldsymbol{r} = A(\boldsymbol{r})$. We apply Schauder's fixed point theorem to obtain a Taylor model for the flow $\mathcal{M}(\boldsymbol{r}_0, t)$ of the ODE (2.6). An important aspect is that the quantity $\boldsymbol{r}_0$ in the fixed point problem can be either a point expressed by real numbers, or an interval box, or Taylor models depending on the initial conditions, or a combination of the above.

To apply Schauder's theorem, we follow the following steps.

- Determine a family Y of subsets of X, the Schauder Candidate Sets. Each set in Y should be compact and convex, it should be contained in a suitable Taylor model, and its image under A should be in Y. The mathematical details of the choice of the candidate sets are described in [17].

- Using differential algebraic methods on Taylor models, we determine an initial set $M_0 \in Y$ satisfying the inclusion property $A(M_0) \subset M_0$. Then all requirements of Schauder's theorem are satisfied, and M_0 contains a solution. Note that different from other verified integrators, in this procedure we simultaneously determine the so-called a priori (initial) inclusion as well as the high order inclusion necessary to execute the step.

- Iteratively generate the sequence $M_i = A(M_{i-1})$ for $i = 1, 2, ...$ Each M_i also satisfies $A(M_i) \subset M_i$, and we have $M_1 \supset M_2 \supset \dots$. We continue the iteration until the size stabilizes sufficiently.

For computational purposes, the only requirement for Schauder's theorem is to find a Taylor model $\boldsymbol{P} + \boldsymbol{I}$ such that

$$A(\boldsymbol{P} + \boldsymbol{I}) \subset \boldsymbol{P} + \boldsymbol{I}, \tag{2.14}$$

which can be checked computationally. The task depends on finding a suitable choice for $\boldsymbol{P}$ and $\boldsymbol{I}$, and furthermore it is desirable to have $\boldsymbol{I}$ as tight as possible. By choosing a polynomial $\boldsymbol{P}$ that is already close to the true solution of the ODE in the following way, we can get the desired answer.

The n-th order expansion $\mathcal{M}_n(\boldsymbol{r}_0, t)$ of the flow including time dependence can be obtained in conventional Differential Algebraic scheme [4]. Choose an initial function $\mathcal{M}_n^{(0)}$ to be the identity function $\mathcal{I}$, then iteratively determine

$$\mathcal{M}_n^{(k+1)} =_n A(\mathcal{M}_n^{(k)}). \tag{2.15}$$

This process converges to the exact result $\mathcal{M}_n$ in $n + 1$ steps.

Now try to find $\boldsymbol{I}^*$ such that

$$\mathcal{M}_n + \boldsymbol{I}^* \subset A(\mathcal{M}_n + \boldsymbol{I}^*), \tag{2.16}$$

the Schauder inclusion requirement. The suitable choice for $\boldsymbol{I}^*$ requires some trial and error. $\boldsymbol{I}^{(0)}$ obtained as $A(\mathcal{M}_n + [\boldsymbol{0}, \boldsymbol{0}]) = \mathcal{M}_n + \boldsymbol{I}^{(0)}$ can serve as a good estimate for a lower bound for $\boldsymbol{I}^*$ because $\boldsymbol{I}^* \supset \boldsymbol{I}^{(0)}$. Now iteratively try $\boldsymbol{I}^{(k)} = q^k \cdot \boldsymbol{I}^{(0)}$ with $q > 1$, until a computational inclusion is found, i.e. $A(\mathcal{M}_n + \boldsymbol{I}^{(k)}) \subset \mathcal{M}_n + \boldsymbol{I}^{(k)}$. In practice, a computational inclusion can be found in a few iterations with q between 1 and 2. Should this however not be the case, it can almost always be forced by slightly reducing the integration step size, which reduces the main contribution of the remainder bound of the mapped set.

Once a computational inclusion has been determined, the solution of the ODE is known to be contained in the Taylor model $\mathcal{M}_n + \boldsymbol{I}^{(k)}$. Set $\boldsymbol{I}_{(1)} = \boldsymbol{I}^{(k)}$. Since the solution is a fixed point of A, it is even contained in $A^k(\mathcal{M}_n + \boldsymbol{I}_{(1)})\ \forall k$. Furthermore, the iterates of A are shrinking in size, i.e. $A^k(\mathcal{M}_n + \boldsymbol{I}_{(1)}) \subset A^{k-1}(\mathcal{M}_n + \boldsymbol{I}_{(1)})\ \forall k$. So the width of the remainder bound of the flow can be decreased by iteratively determining $\mathcal{M}_n + \boldsymbol{I}_{(k)} = A(\mathcal{M}_n + \boldsymbol{I}_{(k-1)})$, until no further significant decrease in size is achieved. As a result, $\mathcal{M}_n + \boldsymbol{I}_{(k)}$ is the desired sharp inclusion of the flow of the ODE.

To integrate over time, we apply the procedure at each time step. Automatic step size controllers are utilized that assure that if the solution at a

time step is not favorable, the step size is decreased, on the other hand, if a time step can proceed without much growth of errors, the next step size is increased.

In order to improve the accurate representation of flows and to prevent the growth of the remainder bound when applied to the celestial mechanics, shrink wrapping and preconditioning are implemented.

Shrink Wrapping

Shrink wrapping [18] is a method to control the long-term growth of integration errors in Taylor model-based integrations. For a fixed time t of interest, the errors appearing in the remainder interval can at least in principle be kept as small as desired by increasing the expansion order n. However, for large values of the time t, this approach may become computationally impractical because the compounding of errors can be rapid, and so it is desirable to develop schemes that limit the error growth as a function of time for a fixed expansion order and computational accuracy. The shrink wrapping serves this purpose. It is based on the idea of enclosing the remainder error including floating point errors and errors due to the finite order in time within the range of the polynomial part of the Taylor model. By doing so, the remainder error ceases to be an interval, and instead is transformed into a variable that is retained explicitly up to the order of the Taylor model. The improvements reachable with respect to a classical Taylor model integrator are shown by applying it to the following two-state discrete dynamical system:

$$\begin{aligned} x_{n+1} &= x_n \cdot \sqrt{1 + x_n^2 + y_n^2} \quad \text{and} \quad y_{n+1} = y_n \cdot \sqrt{1 + x_n^2 + y_n^2} \\ x_{n+2} &= x_{n+1} \cdot \sqrt{\frac{2}{1 + \sqrt{1 + 4(x_{n+1}^2 + y_{n+1}^2)}}} \text{ and} \\ y_{n+2} &= y_{n+1} \cdot \sqrt{\frac{2}{1 + \sqrt{1 + 4(x_{n+1}^2 + y_{n+1}^2)}}}. \end{aligned} \tag{2.17}$$

Simple arithmetic shows that this transformation has the property that $(x_{n+2}, y_{n+2}) = (x_n, y_n)$. Considering the action of the system on the box $[-d, d]^2$, we see that the corner points $(\pm d, \pm d)$ are stretched out more than the axis intersection points $(\pm d, 0)$ and $(0, \pm d)$, which leads to a pincushion shape with four-fold symmetry after each odd step; the action on three centered squares is shown in Figure 2.3. Attempting to represent this structure by an interval box, or for that matter any linear transformation of an interval box, will thus necessarily lead to a noticeable overestimation. On

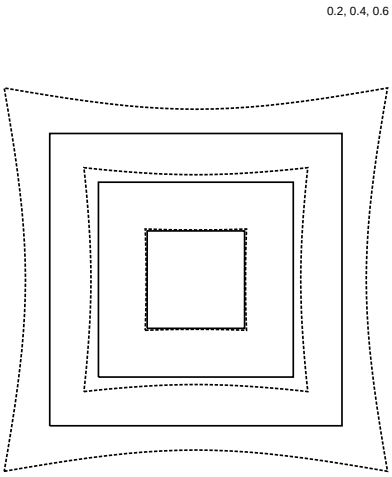

Figure 2.3: The action of the two-step nonlinear transformation. Squares are subjected to pincushion-shaped deformation and transformed back into themselves.

the other hand, representing the action of the iteration by a Taylor model will, for moderate values of d, be able to lead to a much more accurate representation. Finally, note that the linear transformations of the action of this system will always return to the identity after even numbers of iteration and is also rather well conditioned after odd iterations, so numerical difficulties due to conditioning do not arise in this case. Thus the example represents a good test for a method to treat nonlinear effects.

The results of a simulation with Taylor models of various orders and with and without shrink wrapping are shown in Figures 2.4 and 2.5 for the point $(0,0)+[-.05,.05]^2$ and in Figure 2.6 and 2.7 for the point $(1,1)+[-.05,.05]^2$. Because after two steps the linear part is the identity, the problem allows the study the ability of the shrink wrapping method to handle nonlinear effects, but without possible complications that may arise due to the conditioning of the linear part.

Apparently the use of shrink wrapping and higher order Taylor models leads to very extended stability; for example, Taylor models of order 20 lead to survival for 10^5 iterations with an accumulated error around 10^{-9}, while the lack of use of shrink wrapping or the use of linear methods leads to unacceptable errors in 100 or less iterations.

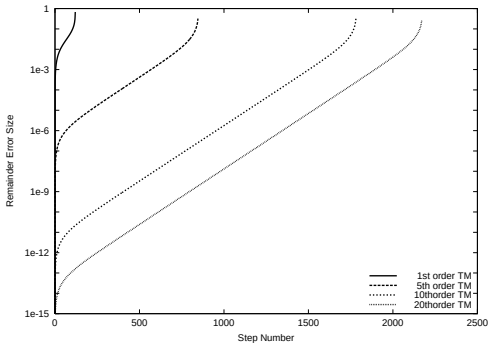

Figure 2.4: Discrete dynamics of the nonlinear stretch at $(0,0) + [-.05,.05]^2$. Treatment by naive Taylor models.

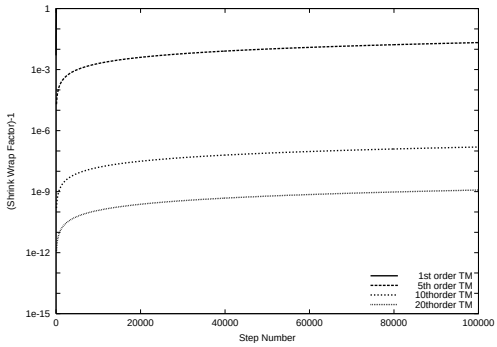

Figure 2.5: Discrete dynamics of the nonlinear stretch at $(0,0) + [-.05,.05]^2$. Treatment by Taylor models with shrink wrapping.

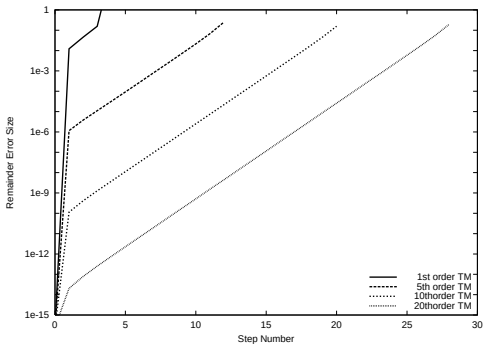

Figure 2.6: Discrete dynamics of the nonlinear stretch at $(1,1) + [-.05,.05]^2$. Treatment by naive Taylor models.

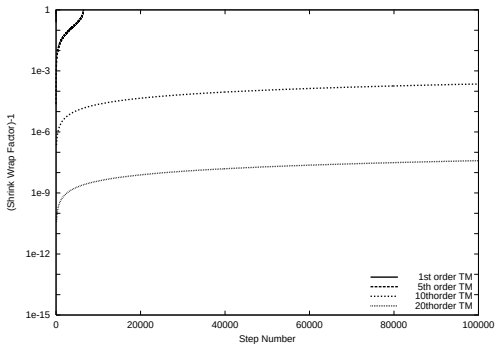

Figure 2.7: Discrete dynamics of the nonlinear stretch at $(1,1) + [-.05,.05]^2$. Treatment by Taylor models with shrink wrapping.

Preconditioning

Preconditioning [19] is proposed to affect the behavior of the remainder bounds of the solutions of ODE. The idea is to write the Taylor model of the solution as a composition of two Taylor models $(P_l + I_l)$ and $(P_r + I_r)$, and then choose $P_l + I_l$ in such a way that I_l is zero up to roundoff, and the operations appearing on I_r are minimized so as not to increase the size of I_r significantly. In a wider context, the Taylor model $(P_l + I_l)$ can be viewed as a specific coordinate system in which the motion is studied. For practical purposes, in the factorization we impose that $(P_r + I_r)$ is normalized such that each of its components has a range in $[-1, 1]$; for purposes of numerical

stability, it is advantageous that the range is in fact near $[-1, 1]$. This is achieved by factoring out a linear diagonal transformation containing scaling factors. Several kinds of preconditioning methods have been recently developed and tested for discrete and continuous dynamical systems. The results given in the following example consider curvilinear and QR preconditioning. For details on these two methods see [19].

The beneficial effect of this technique is here shown for a discrete system that describes the dynamics of circular Kepler orbits around a central mass in terms of the variables (x, y) in the plane of the motion. It is well known from Kepler's third law that the periods T and semi-major axes a of a Kepler ellipse are related via $T^2 = k \cdot a^3$, where k is determined by the mass of the central object. For circular orbits of radius r, for $k = 1$ this entails an angular velocity of $\omega = 2\pi/T = 2\pi \cdot r^{-3/2}$, which means that the transformation by a fixed time step Δt is given by the two-dimensional transformation

$$\begin{pmatrix} x_{n+1} \\ y_{n+1} \end{pmatrix} = \begin{pmatrix} \cos\Delta\phi & \sin\Delta\phi \\ -\sin\Delta\phi & \cos\Delta\phi \end{pmatrix} \begin{pmatrix} x_n \\ y_n \end{pmatrix}$$
$$\text{where } \Delta\phi = \frac{2\pi\Delta t}{(x^2+y^2)^{3/4}}.$$

While addressing only circular motion, the dynamics are also quite characteristic of the general motion of Kepler ellipses because it captures one of the main effects; as time progresses, there is a larger and larger lag between the circles of different radii r. This lag makes Taylor expansion of final conditions in terms of initial conditions impossible for sufficiently large times, and thus represents a challenge for all Taylor-based methods that will necessarily lead to their eventual failure. The interest in the problem now lies in the attempt to delay failure.

Figure 2.8 shows the remainder bounds of the study of the dynamics without shrink wrapping for repeated application of the discrete transformation with $\phi_0 = \pi/4$; in which case one full revolution, or one cycle, consists of eight applications of the individual map.

As a reference we use first order Taylor models preconditioned by curvilinear coordinates. We compare this with tenth order Taylor models preconditioned by curvilinear coordinates, and tenth order Taylor models preconditioned by the QR method. The growth of the remainder bounds is shown for four different initial domain widths of 10^{-6}, 10^{-8}, 10^{-10}, and 10^{-12} as a function of full cycles of 2π. It can be seen that for each case, the tenth order Taylor model method survives between 7 and 10 times longer than the first order method. Furthermore, the preconditioning by curvilinear coordinates

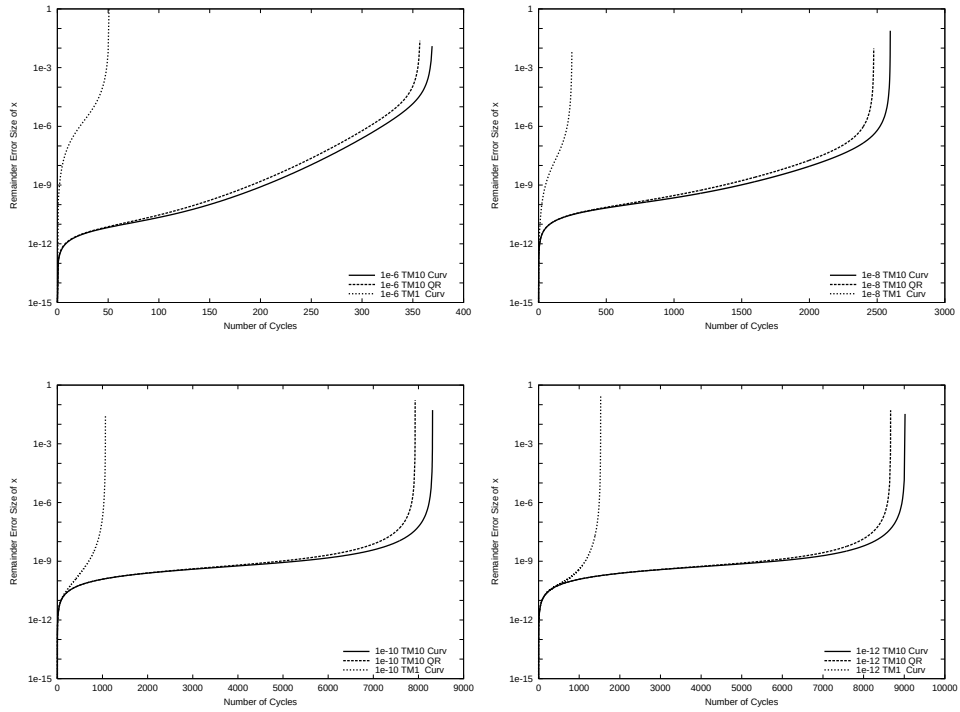

Figure 2.8: Dynamics in the discrete 2D Kepler system for initial box sizes widths of 10^{-6} (top left), 10^{-8} (top right), 10^{-10} (bottom left) and 10^{-12} (bottom right). Shown are the remainders obtained by the first and tenth order Taylor method using Curvilinear Preconditioning and QR preconditioning.

leads to a slightly better performance, which is attributed to the fact that the movement of the coordinate system is smoother since it follows the reference orbit instead of the somewhat more random orientation of the longest edge.

It is also interesting to estimate the growth rate of the remainder bounds in the high-order TM methods. An inspection of the bottom right picture in Figure 2.8 reveals that during revolutions 1000 and 6000, the remainder width increases from about 10^{-10} to about 10^{-9}, for a total increase of $9 \cdot 10^{-9}$ over $5,000$ revolutions or $40,000$ iterations. This corresponds to about $2 \cdot 10^{-13}$ per map iteration; considering that each iteration requires several function evaluations, and that in our current implementation, this number is very close to the unavoidable consequences of accounting for the mere floating point errors of the arithmetic involving the constant part of the Taylor model.

2.4.2 New Validated Integration Tool

In the following subsection, we briefly describe the main features implemented in the new validated integrator. For details refer to [20].

Flow Operator

Referring to the ODE 2.6, the first step is to obtain the Taylor expansion in time of the solution of ODE of center point c, i.e. obtain

$$\boldsymbol{c}(t) = \boldsymbol{c}_0 + \boldsymbol{c}_1(t-t_0) + \boldsymbol{c}_2(t-t_0)^2 + \cdots + \boldsymbol{c}_n(t-t_0)^n \tag{2.18}$$

by n iterations of the Picard Operator

$$\boldsymbol{c}(t) = \boldsymbol{c}_0 + \int_0^t \boldsymbol{f}(\boldsymbol{r}(t'), t)dt' \tag{2.19}$$

in one-dimensional Taylor arithmetic. Each iteration raises the order by one; so in each iteration i, we only need to do Taylor arithmetic in order i. In either way, this step is cheap since it involves only one-dimensional operations.

The goal of the second step is to obtain Taylor expansion in time to order n and initial conditions to order k. This is usually the most expensive step. In the original Taylor model-based algorithm, it is done by n iterations of the Picard Operator in multi-dimensional Taylor arithmetic, where $\boldsymbol{c}_0$ is now a polynomial in initial conditions. To improve this step we introduce a perturbation variable $\bar{r}(t)$ such that

$$\boldsymbol{r}(t) = \boldsymbol{c}(t) + A \cdot \bar{\boldsymbol{r}}(t), \tag{2.20}$$

such that the matrix A provides preconditioning. The ODE for $\bar{r}(t)$ are

$$\bar{\boldsymbol{r}}' = A^{-1}[\boldsymbol{f}(\boldsymbol{c}(t) + A \cdot \bar{\boldsymbol{r}}(t)) - \boldsymbol{c}'(t)]. \tag{2.21}$$

We then evaluate the ODE for $\bar{\boldsymbol{r}}'(t)$ in Taylor arithmetic thus obtaining a Taylor expansion of the ODE, i.e. $\bar{\boldsymbol{r}}' = \boldsymbol{P}(\bar{\boldsymbol{r}}, t)$, up to order n in time and k in $\bar{r}$. It is important that $\boldsymbol{P}$ has no constant part, i.e. $\boldsymbol{P}(0,t) = 0$. The n-th order expansion of the flow can be computed by applying Lie derivative

$$\bar{\boldsymbol{r}}(t) = \sum_{i=0}^{n} \frac{(t-t_0)^i}{i!} \cdot \left(\boldsymbol{P} \cdot \nabla + \frac{\partial}{\partial t}\right)^i \bar{\boldsymbol{r}}_0/_{t=t_0}. \tag{2.22}$$

Note that the fact that $\boldsymbol{P}(0,t) = 0$ restores the derivatives lost in ∇ and that, by appearing without origin preserving factor, $\partial/\partial t$ limits the expansion order to n. Apparently we have the following results

1. Each term in the Lie derivative sum requires $v+1$ derivations (very cheap, just reshuffling of coeffcients)
2. Each term requires v multiplications
3. One evaluation of $\boldsymbol{f}$ in ${}_nD_v$ (to set up ODE) is needed.

By comparing this algorithm with the conventional algorithm, which requires n evaluations of the function $\boldsymbol{f}$ of the right hand side, we can conclude that if the evaluation of $\boldsymbol{f}$ requires more than v multiplications, the new method is more efficient. Note that many practically appearing right hand sides $\boldsymbol{f}$, including Solar System dynamics, have this property. On the other hand, if the function $\boldsymbol{f}$ does not satisfy this (for example for the linear case), then also $\boldsymbol{P}$ will be simple (in the linear case: $\boldsymbol{P}$ will be linear), and thus less operations appear.

Step Size Control

Step size control is used to maintain approximate error ε in each step. The procedure adopted to achieve this goal is the following:

1. Utilize the reference orbit. Extrapolate the size of coefficients to estimate the remainder error, scale so that it reaches and get Δt_1.
2. Utilize the flow. Compute flow time step with Δt_1. Extrapolate the contributions of each order of flow for estimate of remainder error to get update Δt_2.
3. Utilize a correction factor $c = (|\boldsymbol{R}|/\varepsilon)^{\frac{1}{(n+1)}}$.
4. Perform verification attempt for $\Delta t_3 = c\Delta t_2$.

Dynamic Domain Decomposition

For extended domains, this is natural equivalent to step size control. The procedure is the following:

1. Evaluate ODE for $\Delta t = 0$ for current ow.
2. If the resulting remainder bound $\boldsymbol{R}$ is greater than ε, split the domain along variable leading to longest axis.
3. Absorb $\boldsymbol{R}$ in the Taylor model polynomial part. If it fails, split the domain along the variable leading to the largest x dependence of the error.

4. Put one half of the box on stack for future work.

Note that the "First-in-last-out"stack is used to minimize stack length. Special adjustments for stack management in a parallel environment, including load balancing are implemented too. Furthermore, dynamic order control for dependence on initial conditions is included.

Chapter 3

Models

This chapter describes the dynamical models and ephemeris functions developed to perform the integration of Apophis asteroid. Two different dynamical models are introduced to compute the heliocentric and geocentric phases of the trajectory, and three different ephemeris functions are implemented to describe the dynamics with different degrees of accuracy.

3.1 Dynamical Models

In order to integrate the motion of Apophis with high accuracy, two main dynamical models are adopted. In the first one the dynamics are written in the J2000.0 coordinates, in which the x axis is aligned with the mean equinox at the given reference epoch and the z axis is orthogonal to the ecliptic plane. The second one is written in a reference frame centered in the Earth's center of mass, having the x axis aligned with the mean equinox at the reference epoch and the z axis orthogonal to the equatorial plane.

3.1.1 Solar System Barycentric Restricted $(n+1)$-Body Problem

The study of the motion of a near Earth object (NEO) in the Solar System with an accuracy sufficient to predict collisions requires the inclusion of various relativistic corrections to the well-known Newtonian forces based on the Kepler's force law. Specifically, the full equation of motion in the solar system including the relevant relativistic effects is given by

$$\ddot{\boldsymbol{r}} = G\sum_i \frac{m_i(\boldsymbol{r}_i - \boldsymbol{r})}{r_i^3}\left\{1 - \frac{2(\beta+\gamma)}{c^2}G\sum_j \frac{m_j}{r_j} - \frac{2\beta-1}{c^2}G\sum_{j\neq i}\frac{m_j}{r_{ij}} + \frac{\gamma|\dot{\boldsymbol{r}}|^2}{c^2}\right.$$
$$+ \frac{(1+\gamma)|\dot{\boldsymbol{r}}_i|^2}{c^2} - \frac{2(1+\gamma)}{c^2}\dot{\boldsymbol{r}}\cdot\dot{\boldsymbol{r}}_i - \frac{3}{2c^2}\left[\frac{(\boldsymbol{r}-\boldsymbol{r}_i)\cdot\dot{\boldsymbol{r}}_i}{r_i}\right]^2 + \frac{1}{2c^2}(\boldsymbol{r}_i - \boldsymbol{r})\cdot\ddot{\boldsymbol{r}}_i\Bigg\}$$
$$+ G\sum_i \frac{m_i}{c^2 r_i}\left\{\frac{3+4\gamma}{2}\ddot{\boldsymbol{r}}_i + \frac{\{[\boldsymbol{r}-\boldsymbol{r}_i]\cdot[(2+2\gamma)\dot{\boldsymbol{r}} - (1+2\gamma)\dot{\boldsymbol{r}}_i]\}(\dot{\boldsymbol{r}}-\dot{\boldsymbol{r}}_i)}{r_i^2}\right\}$$
$$+ \boldsymbol{a}_{Yd}, \tag{3.1}$$

where $\boldsymbol{r}$ is the point of interest, $G = 6.67529\times10^{-11}$ m^2/(s^{2}kg) is the gravitational constant; m_i and $\boldsymbol{r}_i$ are the mass and the solar-system barycentric position of body or system i,; $r_i = |\boldsymbol{r}_i - \boldsymbol{r}|$; and β and γ are the parametrized post-Newtonian parameters measuring the nonlinearity in superposition of gravity and space curvature produced by unit rest mass [21].

In Equation 3.1 it is supposed that the object we are integrating is affected by the gravitational attraction of n bodies, but that has no gravitational effect on them, i.e. we are adopting the restricted $(n+1)$-body problem approximation. In our particular integrations n includes the Sun and the nine planets. Note that for planets with moons the center of mass of the system is considered. To improve the integration accuracy the dynamics are scaled by Earth semi-major axis and Sun gravitational parameter (i.e., $a_E = 1$ and $\mu_S = Gm_s = 1$).

We must mention that, to obtain a full understanding of the dynamics of a body in the Solar system, other effects could be taken into account. Among them are: the forces due to other natural satellites and asteroids, the J_2 (and higher order harmonics of the potential) effect of the Earth and other bodies, Yarkovski and solar radiation pressure effects. Only diurnal Yarkovski effect, $\boldsymbol{a}_{Yd}$, [22] is included in the ODE right hand side. The asteroid spin axis is assumed perpendicular to its orbit, which maximizes the diurnal Yarkovsky effect [23].

In this framework the positions, velocities, and accelerations of the n bodies are considered as given values, computed by an ephemeris function. Within this contract, three different models of ephemerides are implemented, characterized by different levels of accuracy and complexity, as described in Sections 3.2.1, 3.2.2, and 3.2.3.

3.1.2 Geocentric Restricted $(n+1)$-Body Problem

In Section 3.1.1 we described the dynamical model used to propagate the NEO motion during the heliocentric phase. When the asteroid approaches the Earth, a different set of ODE are integrated to improve the integration accuracy. These ODE are written in a non-inertial reference frame centered in the Earth center of mass, with the x axis in mean equinox direction and the z axis aligned with Earth spin axis at the reference epoch. The equation of motions are described by

$$\ddot{\boldsymbol{r}} = G\sum_i \frac{m_i(\boldsymbol{r}_i - \boldsymbol{r})}{r_i^3} + \boldsymbol{a}_{Yd} - \ddot{\boldsymbol{r}}_E, \tag{3.2}$$

where $\boldsymbol{r}$ is the point of interest; m_i is the mass and $\boldsymbol{r}_i$ the position with respect to the Earth center of mass of body or system i,; and $\ddot{\boldsymbol{r}}_E$ is the absolute acceleration of the Earth center of mass. Note that here the Earth and the Moon are considered separately, thus $n = 11$. Relativistic effects are neglected as their effect during a fast close encounter are negligible, whereas Earth oblateness is taken into account through J_2 harmonic. To improve the integration accuracy of this phase, the dynamics are scaled by the radius of the Earth and by the Earth gravitational parameter (i.e., $R_E = 1$ and $\mu_E = Gm_e = 1$).

In order to assess the performance of the new validated integrator, a simplified version of the dynamical system is examined. This simplification consists in considering only the Earth and the Sun as attracting bodies, and neglecting the effects due to the Earth oblateness. Furthermore, a simple model of the ephemerides based on osculating ellipses is adopted, as described in Section 3.2.1.

3.2 Ephemeris Models

The ephemeris functions used are based on the DE405 of Caltech's Jet Propulsion Laboratory (JPL) ephemerides. These have been obtained from a least-square fitting of previously existing ephemerides to the available observation data, followed by a numerical integration of a suitable set of equations describing the motion of the Solar System. The numerical integrations were carried out using a variable step-size, variable order Adams method. The result of the integration is stored in form of interpolatory data (Chebyshev polynomials, each block of them covering an interval of 32 days). The DE405

ephemerides are valid from Dec 9, 1599 to Feb 1, 2200 [24]. The internal reference system is the so-called J2000 coordinates, and a detailed description about how these ephemerides are obtained can be found in [25].

As both in the DA and TM framework the planetary ephemerides cannot be computed by external codes, interpolations in time of either planetary states or orbital parameters, obtained trough JPL DE405, are carried out. In particular, three different approximations are considered, as detailed in the following subsections. Note that the result of evaluating the ephemeris function in the DA and TM frame is an arbitrary order Taylor expansion or Taylor model representation of the position and the velocity of the planet with respect to the epoch t.

3.2.1 Osculating Ellipses Approximation

The osculating ellipses ephemeris model is mainly developed for the evaluation of the performances of the new validated integrator. In this model it is supposed that the gravitational bodies move on conic arcs, i.e. their motion is affected only by the gravitational force of the Sun, which is supposed fixed and coinciding with the Solar System barycenter. Within this approximation, five orbital parameters $(a, e, i, \Omega, \omega)$ are constant for each planet, whereas the mean anomaly M varies as

$$M = M_0 + n(t - t_0), \tag{3.3}$$

in which M_0 is the mean anomaly at the reference epoch, n is the mean motion, and $t - t_0$ the elapsed time from the reference epoch. Conversion from orbit elements to cartesian quantities is performed as follows:

$$\begin{array}{rcl} x &=& r[\cos(\vartheta+\omega)\cos\Omega - \sin(\vartheta+\omega)\cos i\sin\Omega] \\ y &=& r[\cos(\vartheta+\omega)\sin\Omega + \sin(\vartheta+\omega)\cos i\sin\Omega] \\ y &=& r[\sin(\vartheta+\omega)\sin i] \\ v_x &=& v[-\sin(\vartheta+\omega-\gamma)\cos\Omega - \cos(\vartheta+\omega-\gamma)\cos i\cos\Omega] \\ v_y &=& v[-\sin(\vartheta+\omega-\gamma)\sin\Omega + \cos(\vartheta+\omega-\gamma)\cos i\cos\Omega] \\ v_z &=& v[\cos(\vartheta+\omega-\gamma)\sin i] \end{array} \tag{3.4}$$

where the velocity v is

$$v = \sqrt{\frac{\mu}{r} - \frac{\mu}{a}}, \tag{3.5}$$

the true anomaly is related to the eccentric anomaly by

$$\tan\frac{E}{2} = \sqrt{\frac{1-e}{1+e}}\tan\frac{\vartheta}{2}, \tag{3.6}$$

the flight path angle is obtained from

$$\tan\gamma = \frac{e\sin\vartheta}{1+e\cos\vartheta}, \tag{3.7}$$

and the eccentric anomaly is related to the mean anomaly by Kepler's equation,

$$M = E - e\sin E. \tag{3.8}$$

Thus, based on the orbital parameters, the cartesian position and velocity of planets are computed as a function of time with only the nuisance of solving the Kepler's equation in a validated way. In order to further simplify the ephemerides evaluation, the solution of the Kepler's equation is substituted by the third expansion in the eccentricity e,

$$E \simeq M + \frac{e\sin M}{1-e\cos M} - \frac{1}{2}\left(\frac{e\sin M}{1-e\sin M}\right)^3 \tag{3.9}$$

introduced by Battin [26]. Such kind of solution turns out to be particularly appropriate in the framework of planetary ephemerides evaluation, since all planetary orbits in the Solar System are characterized by relatively low eccentricity values. The computed eccentric anomaly E is then used to evaluate planetary positions and velocities, through (3.4)–(3.7). The accuracy of this model is too low even for predicting a close encounter, as it will be shown in Chapter 5. On the other hand, it can be used to propagate Apophis flyby, as this phase has short duration and it is mainly driven by the gravitational force of a single body, i.e. the Earth.

3.2.2 Fourier Inetrpolation

The second ephemeris model consists of a Fourier interpolation of cartesian position and velocity of JPL DE405 ephemerides. The interpolation process is done by evaluating, for each planet, the JPL ephemerides on a grid covering the range 1980-2050 AD. This data is then interpolated using either a 8-th order single Fourier interpolation or a double 3-rd order Fourier interpolation of data and associated residuals. Although the interpolants are computed based on data in a specific time window, their validity is global in time. Furthermore, being $\mathcal{C}^\infty$, Fourier interpolants are particularly suitable for DA and TM evaluation.

As shown by Figure 3.1 and 3.2, this model has an accuracy of the order of 10^{-4} AU and 10^{-6} AU/day for Earth's position and velocity, respectively. It has been observed that the accuracy lowers of roughly one order of magnitude

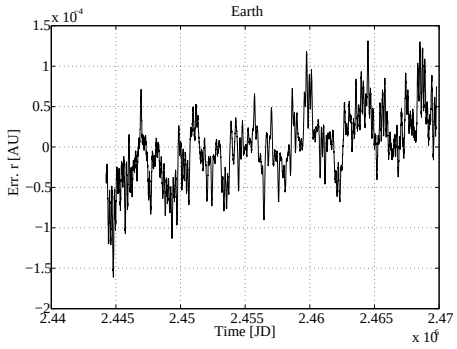

Figure 3.1: Fourier interpolation: errors on Earth position.

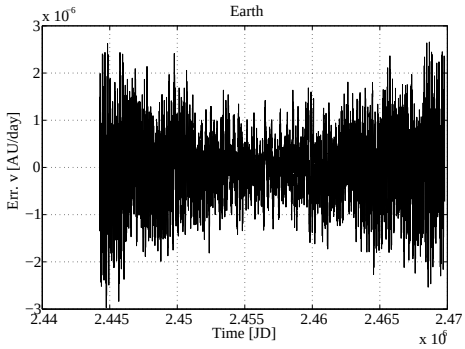

Figure 3.2: Fourier interpolation: errors on Earth velocity.

for Jupiter and Saturn systems. As it will be shown in Section 5.1, these accuracy levels enable the detection of an Apophis–Earth close encounter, but are too low for capturing its details, e.g. the prediction of the Earth's surface close encounter distance (CED) and close encounter epoch.

These limitations could be overtaken by splitting the time window 1980-2050 AD in sub intervals and by increasing the interpolation order, making Fourier ephemerides a promising model within the validated computation framework. Note also that by interpolating the cartesian position and velocity of planets, the problem of validated solution of Kepler's equation is avoided.

For the sake of completeness we report a 3-rd order TM evaluation of the x component of the position and velocity of the Earth in the epoch interval $t \in 5.4788 \times 10^3 + [-10, 10]$ MJD2000. The Taylor model is centered in $t = 5.4788 \times 10^3$ and it has domain $[-1, 1]$, meaning that evaluating the obtained polynomial in ± 1 gives the validate position and velocity at $t = 5.4887 \times 10^3$ and $t = 5.4689 \times 10^3$, respectively.

$x_E = x_E(t)$

```
 I  COEFFICIENT             ORDER EXPONENTS
 1  -.1669075403225326        0   0
 2  -.1723017185415151        1   1
 3  0.2658042461803231E-02    2   2
 4  0.8527372199314997E-03    3   3
 5  -.3378581235471234E-04    4   4
 6  0.9408565734752021E-05    5   5
 7  0.4757141683426523E-05    6   6
 ---------------------------------
REFERENCE POINT 5.4788e+03, DOMAIN       [-1, 1]
```

```
REMAINDER BOUND INTERVAL
 [-.2812801267283755E-005,0.2812801267302219E-005]
```

$v_{xE} = v_{xE}(t)$

```
 I  COEFFICIENT             ORDER EXPONENTS
 1  -.1723011543196994E-01   0   0
 2  0.5316016346735601E-03   1   1
 3  0.2557609427224155E-03   2   2
 4  -.1352806827720667E-04   3   3
 5  0.4762338258916880E-05   4   4
 6  0.2908386066089425E-05   5   5
 7  -.1010927968243084E-05   6   6
 ---------------------------------
REFERENCE POINT 5.4788e+03, DOMAIN       [-1, 1]
REMAINDER BOUND INTERVAL
 [-.7684036281430896E-006,0.7684036281413410E-006]
```

3.2.3 Cubic Spline Interpolation: Solar System Barycentric and Geocentric

The third ephemeris model is based on cubic spline interpolation of cartesian position and velocity of planets evaluated with JPL DE405. More specifically, two different interpolations have been carried out, one for the heliocentric phase of Apophis trajectory and the other for the close encounter phase.

For the heliocentric part of the trajectory, the Solar System barycentric coordinates of Mercury, Venus, and Earth, Mars, Jupiter, Saturn, Neptune, Uranus and Pluto systems are interpolated. The ephemerides of the Sun are computed using the Solar System barycenter definition. In order to assure homogeneous interpolation accuracy, a planet dependent grid is adopted, ranging from 3 days for Mercury and up to 90 for Pluto system. The validity of the interpolation is limited to $2010 - 2050$ AD. The accuracy of the interpolation is shown in Figure 3.3 and 3.4, highlighting that the developed model is suitable for an highly accurate prediction of Apophis's motion.

For the close encounter phase, the ephemerides of the Sun, the nine planets and the Moon are interpolated in the geocentric reference frame. Furthermore, the Solar System barycentric coordinates of the Earth are interpolated to obtain the required $\ddot{\boldsymbol{r}}_E$ of (3.2). The validity of these ephemerides is limited to April 2029, as a fine grid of 0.1 day is necessary to describe the high frequency motion of the Moon.

It is important to stress that, although very accurate, the cubic spline ephemeris model is not suitable for the validated integration of Apophis

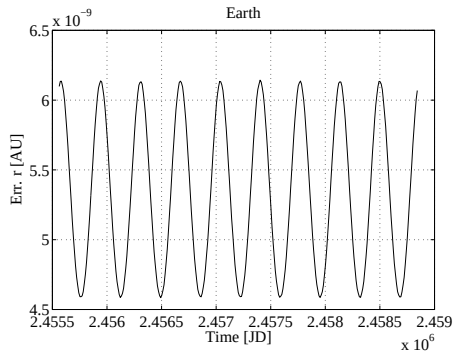

Figure 3.3: Spline interpolation: errors on Earth position.

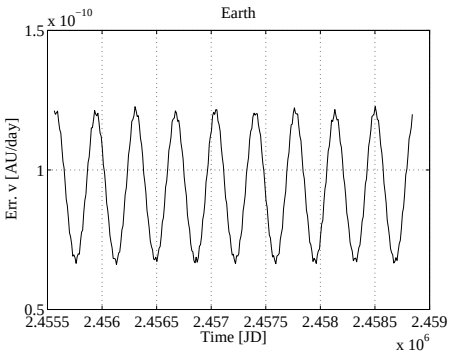

Figure 3.4: Spline interpolation: errors on Earth velocity.

motion. In fact, as the ephemerides are expressed as piecewise continuos functions, validation is not guaranteed when a TM evaluation across a grid node is performed. A possible workaround consists in avoiding grid points that lie inside an integration step, but this expedient would result in a high computational inefficiency. Note that, regardless the selected order of the ephemerides Taylor expansion, the maximum order is three, as a cubic spline interpolation in time is adopted. Here follows the maps for the x component of the position and velocity of the Earth for the same epochs of Section 3.2.2.

$x_E = x_E(t)$

```
 I  COEFFICIENT             ORDER EXPONENTS
 1  -.1668382667210500        0   0
 2  -.1723475696166245        1   1
 3  0.2596105729659144E-02    2   2
 4  0.8894293374598657E-03    3   3
 ---------------------------------
REFERENCE POINT 5.4788e+03, DOMAIN       [-1, 1]
REMAINDER BOUND INTERVAL
[-.6603169961356184E-013,0.6603169961356184E-013]
```

$v_{xE} = v_{xE}(t)$

```
 I  COEFFICIENT             ORDER EXPONENTS
 1  -.1723477570411781E-01    0   0
 2  0.5191942894692477E-03    1   1
 3  0.2683614238116466E-03    2   2
 4  -.3298742894898756E-05    3   3
 ---------------------------------
```

```
REFERENCE POINT 5.4788e+03, DOMAIN       [-1, 1]
REMAINDER BOUND INTERVAL
[-.3981013803778868E-015,0.3981013803778868E-015]
```

Chapter 4

DA-Based Tools for Close Encounter Analysis

This chapter presents the DA-Based tools and the results obtained for the analysis of Apophis trajectory. All the tools are based on the Taylor expansions of the flow of ODE and on map operations, like composition and inversion, built in COSY-Infinity.

4.1 High Order Expansion of ODE Flow

The high order expansion of the flow of ODE can be straightforwardly obtained by evaluating any explicit numerical integration scheme within the DA framework, as explained in Section 2.2. The results presented in this section are obtained with a DA 8-th order Runge–Kutta–Fehlberg (RKF78) with absolute and relative tolerance of 10^{-12}. The dynamical models used are those described in Section 3.1.2 and 3.1.1 for heliocentric and close approach phases, together with cubic spline ephemerides. The integration window is $[7.3179 \times 10^3, 1.0699 \times 10^4]$ MJD2000 corresponding to January 13, 2020 and April 16, 2029. Apophis' nominal initial state, expressed either as orbital parameters or cartesian coordinates, are taken from the JPL Horizons system. The uncertainties associated with orbital element determination are taken from JPL Near Earth Object Program website (at the link http://neo.jpl.nasa.gov/neo/). On the other hand, 3σ values comparable to those in [29] are considered when uncertainties on cartesian coordinates are analyzed. Table 4.1 and in Table 4.2 summarize these informations.

In order to obtain the Taylor expansion of the flow it is necessary to initialize the initial conditions as DA variables. The nominal initial conditions and the associated uncertainty values are used to achieve this goal. In par-

Table 4.1: Apophis' set of nominal initial orbital parameters and associated uncertainty values.

	Nom Value	3σ	
a_0	$9.363669510494852 \times 10^{-1}$	6.885×10^{-8}	AU
e_0	$1.936876472820932 \times 10^{-1}$	2.2335×10^{-7}	–
i_0	$5.781042510494677 \times 10^{-2}$	$1.058193125484162 \times 10^{-7}$	rad
Ω_0	3.566849112857637	$5.592034923389831 \times 10^{-6}$	rad
ω_0	2.250090019038626	$5.544911033585984 \times 10^{-6}$	rad
E_0	1.790307191578179	$2.911732791102140 \times 10^{-6}$	rad

Table 4.2: Apophis' set of nominal initial cartesian coordinates and associated uncertainty values.

	Nom Value	c	
x_0	$5.950831296389420 \times 10^{-2}$	1×10^{-7}	AU
y_0	$9.727658263902151 \times 10^{-1}$	1×10^{-7}	AU
z_0	$-4.986352237979162 \times 10^{-2}$	1×10^{-7}	AU
v_{x0}	$-1.650202028201318 \times 10^{-2}$	6×10^{-9}	AU/day
v_{y0}	$4.212736011207589 \times 10^{-3}$	6×10^{-9}	AU/day
v_{z0}	$-6.161074653433205 \times 10^{-4}$	6×10^{-9}	AU/day

ticular, when the initial conditions are expressed via orbital parameters, the DA initialization is

$$\begin{array}{rcrcl} a & = & a_0 & + & 3\sigma_a\,\delta a \\ e & = & e_0 & + & 3\sigma_e\,\delta e \\ i & = & i_0 & + & 3\sigma_i\,\delta i \\ \Omega & = & \Omega_0 & + & 3\sigma_\Omega\,\delta\Omega \\ \omega & = & \omega_0 & + & 3\sigma_\omega\,\delta\omega \\ E & = & E_0 & + & 3\sigma_E\,\delta E. \end{array} \tag{4.1}$$

The orbital parameters values are then converted into cartesian coordinates by evaluating Equations (3.4)–(3.7) in the DA frame. The result is the n-th order Taylor expansion of the Cartesian coordinates with respect to the orbital parameters

$$\begin{array}{rcl} \boldsymbol{r} & = & \mathcal{M}(a, e, i, \Omega, \omega, E) \\ \dot{\boldsymbol{r}} & = & \mathcal{M}(a, e, i, \Omega, \omega, E) \end{array} \tag{4.2}$$

that can be supplied as initial condition to the DA-RKF integration scheme.

Alternatively it is possible to directly consider the initial conditions in cartesian coordinates and initialize them as DA variables using the values of Table 4.2, resulting in

$$\begin{array}{rcccl} x & = & x_0 & + & c_x\,\delta x \\ y & = & y_0 & + & c_y\,\delta y \\ z & = & z_0 & + & c_z\,\delta z \\ v_x & = & v_{x0} & + & c_{v_x}\,\delta v_x \\ v_y & = & v_{y_0} & + & c_{v_y}\,\delta v_y \\ v_z & = & v_{z0} & + & c_{v_z}\,\delta v_z. \end{array} \tag{4.3}$$

Based on the type of initial condition selected, the result is the n-th order Taylor expansion of the final condition with respect to initial orbital parameters (first approach) or cartesian coordinates (second approach). For the heliocentric phases the computed trajectory is shown in Figure 4.1, in which the green line is the trajectory of the Earth, and the blue and the black lines Apophis trajectory computed with COSY-Infinity and taken from JPL Horizons systems.

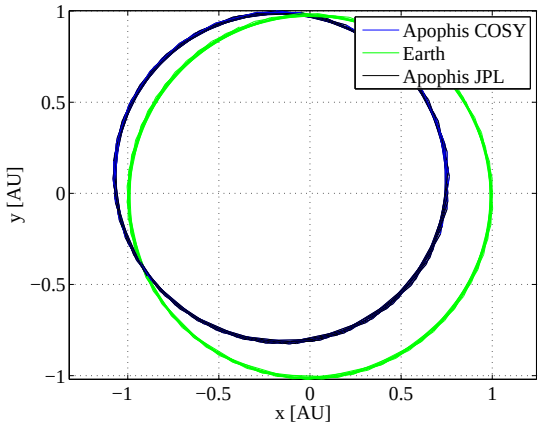

Figure 4.1: Apophis trajectory: heliocentric phase.

The accuracy of the integration is better shown in Figure 4.2. This plot is obtained by splitting the integration into pieces and comparing the nominal values with JPL data. It is shown that the adopted dynamical model and cubic spline ephemerides are appropriate for long-term integration of the asteroid's motion. After roughly ten years of integration the errors on the position are of order of 10^{-7} AU on position, a value low enough to allow an accurate prediction of the details of the close encounter.

Figure 4.3 displays the profile of the errors when the relativistic effects are neglected. More then one order of magnitude is lost, showing the importance of these terms when long-term integrations are addressed.

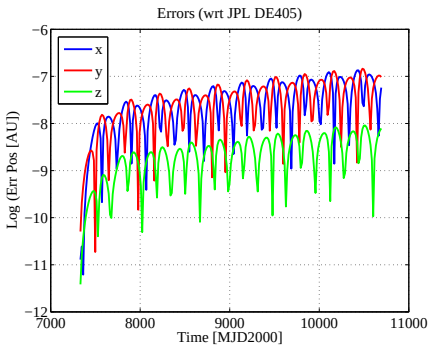

Figure 4.2: Heliocentric phase integration errors.

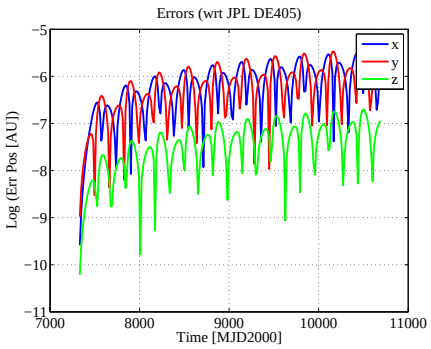

Figure 4.3: Heliocentric phase integration errors neglecting relativistic effects.

Figure 4.4 and 4.5 show Apophis' close approach trajectory integrated in the geocentric reference frame. The blue line is the nominal solution and the black shapes are the envelopes of the cluster of points obtained by evaluating the Taylor expansions of the flow at different epochs. It is clearly shown how the nonlinear dynamics stretches the initial box. In particular, internal points with low velocity are greatly bent by the Earth's gravitational field, whereas the trajectories of external and fast points are less effected. Note that the dotted sphere in the figure represents the Earth's sphere of influence.

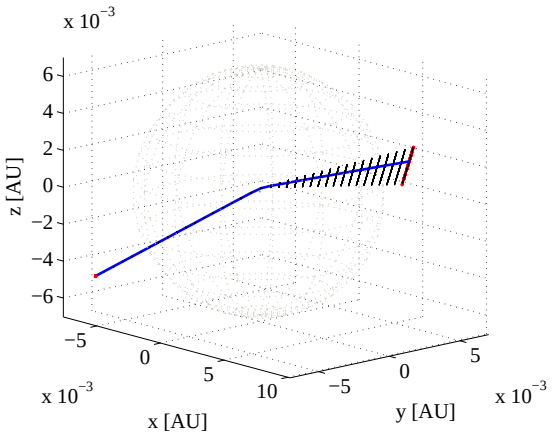

Figure 4.4: 3D plot of geocentric phase of Apophis trajectory.

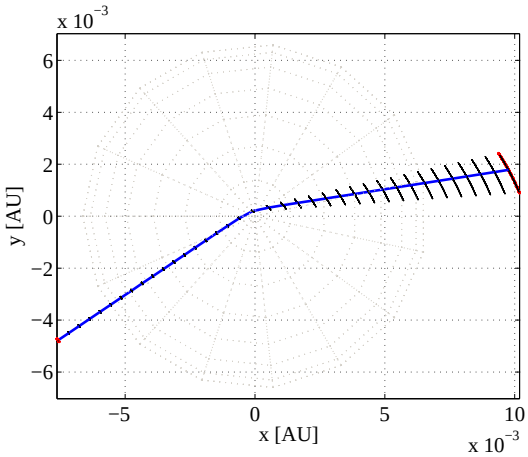

Figure 4.5: Geocentric phase of Apophis trajectory, $x - y$ projection.

Figure 4.6 gives the details of flow evaluation at three different epochs, being $t = 10695.90710$ MJD2000 the epoch in which the nominal asteroid is at 31781.2 km from Earth's surface, i.e. at its CED. The flow evaluations displayed in the picture are relative to uncertainties on cartesian coordinates. As it will be shown in next section, considering the uncertainties on the initial orbital parameters reduces significantly the fan of possible solutions. Figure 4.7 shows the integration accuracy during the flyby. It is clear that the integration error for the reference solution is low until the closest approach, whereas a steep increase of the error occurs in the remaining part of the flyby. Based on this observation, it is important to stress that all the methods presented in the last section for resonant returns analysis suffer this decrease of accuracy, which can jeopardize the results.

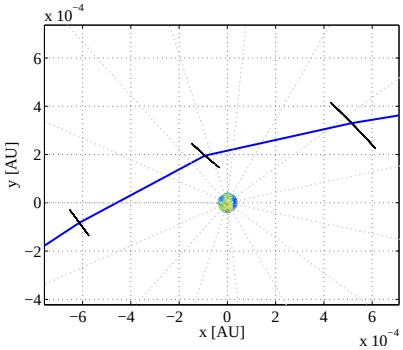

Figure 4.6: Apophis close encounter details.

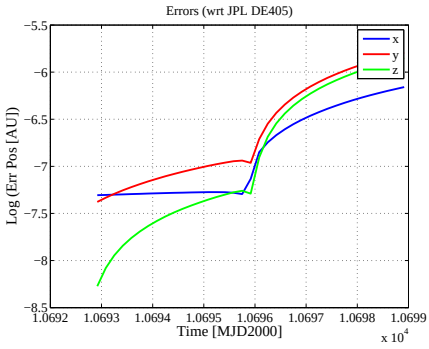

Figure 4.7: Apophis close encounter integration errors.

The results displayed so far refer to a third order expansion of the flow. Figures 4.8 and 4.9 show the maximum position and velocity error of the Taylor representation of the flow at the corners of the initial set, with respect to the pointwise integration of the same points. As it can be seen, the error decreases when higher expansion orders are used. The third order guarantees an error of the order of 10 km for the position and 10^{-2} km/s for the velocity; i.e. it is enough accurate to perform close encounter analysis.

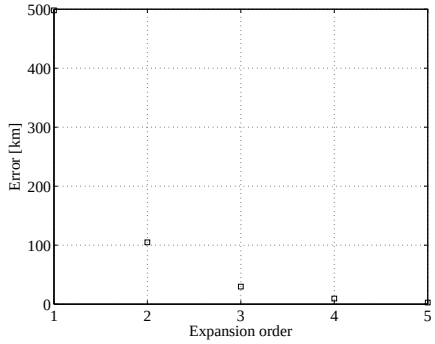

Figure 4.8: Accuracy of the Taylor expansion of the flow corresponding to different expansion orders: position error.

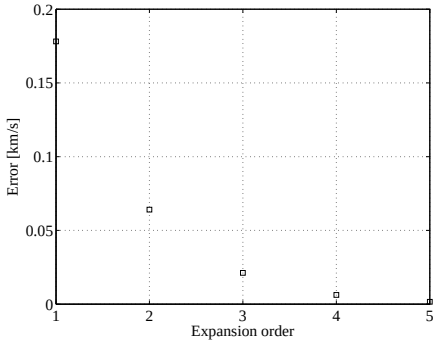

Figure 4.9: Accuracy of the Taylor expansion of the flow corresponding to different expansion orders: velocity error.

Figure 4.10 shows the computational cost of an n-th order ($n = 1 \dots 6$) DA integration compared to a pointwise integration. From this picture it is

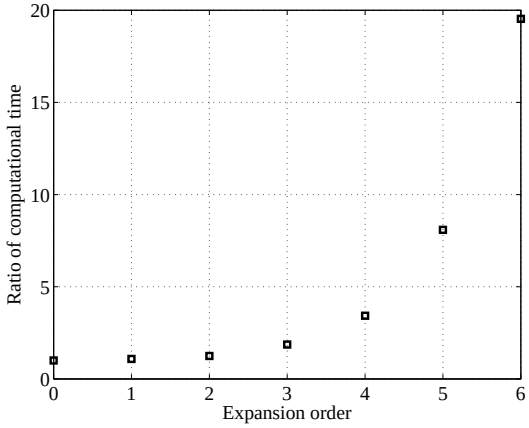

Figure 4.10: DA integration computational time compared to pointwise integration

clear that a third order expansion is a good compromise between integration accuracy and computational cost.

4.2 Improved Monte Carlo Algorithm

A Monte Carlo simulation that exploits the high order expansion of the flow of ODE is presented. As stressed in previous publications on this topic [27], one of the major drawbacks of applying Monte Carlo simulation in estimating the probability of NEO impacts is the computational cost required to propagate thousands initial conditions, the so-called virtual asteroids.

In the previous section it was shown that a single DA integration delivers an arbitrarily order Taylor expansion of the flow of the ODE in a computational time comparable with a pointwise integration. Furthermore, it was remarked that the initial conditions of the asteroid are well within the convergence region of a 3-rd order Taylor expansion of the flow. For this reason, it is possible to substitute the thousands pointwise integrations with an equal number of map evaluations, i.e. fast polynomials evaluations. The computational cost of a Taylor map evaluation depends on the expansion order and ranges from 10^{-7} to 10^{-6} times a pointwise integration. Thus the computational time of a DA-based Monte Carlo simulation is mainly driven by the time required to compute the flow expansion.

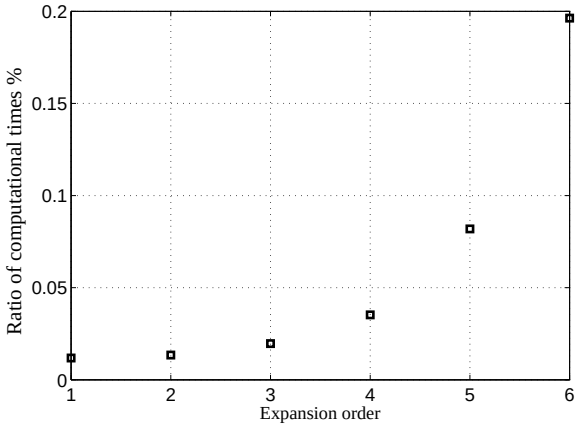

Figure 4.11: Computational time comparison: percentage of computational time required by DA-based Monte Carlo versus a classical Monte Carlo simulation for 10000 virtual asteroids.

Figure 4.11 shows a comparison between the computational time required by a DA-based Monte Carlo simulation and a pointwise Monte Carlo simu-

lation of 10000 virtual asteroids. As the cost of a map evaluation is almost negligible, when the number of samples is lower than one million, the ratio between Monte Carlo simulation computational times can be approximated as $\frac{m}{n_s}$, where m is the ratio between the computational times of an n-th order DA integration and a pointwise integration, and n_s the number of virtual asteroids. Note that the computational cost of a 3-rd order Monte Carlo simulation is approximately the 0.02% of a pointwise one, without a significant loss of accuracy.

Two different Monte Carlo simulations are performed, the first one is based on the uncertainties on orbital parameters and the second one on cartesian coordinates. When the orbital parameters are considered, the virtual asteroids are generated according to the 3σ values shown in previous section, whereas in the case of cartesian coordinates the scaling coefficients of the DA variables — the c coefficients — are assumed as 3σ values.

Figure 4.12 and 4.13 show the virtual asteroids generated for the Monte Carlo simulations. In red we have the virtual asteroids generated with the statistics on the orbital parameters and in black those based on initial cartesian coordinate uncertainties. From these pictures, the initial set based on

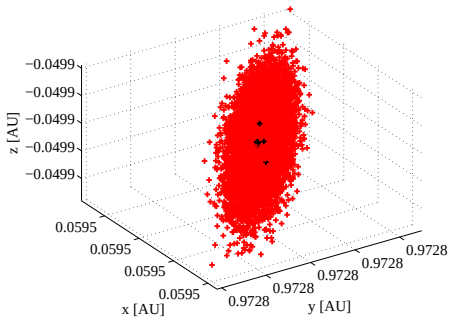

Figure 4.12: Virtual asteroids initial positions based on orbital parameters (red) and cartesian coordinates (black).

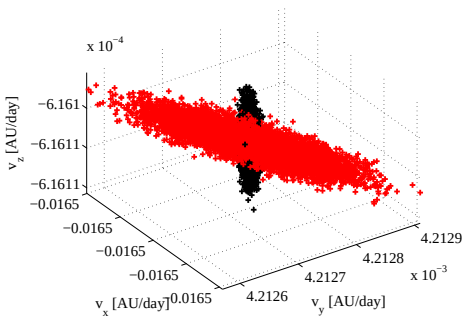

Figure 4.13: Virtual asteroids initial velocities based on orbital parameters (red) and cartesian coordinates (black).

the orbital parameters seems to be wider than that based on the cartesian coordinates. Nevertheless the functional relation of Eq. (4.2) leads to a volume of virtual asteroids that is smaller than that obtained in cartesian coordinate. This result is clearly depicted in Figure 4.14, in which the expansion of the flow is evaluated at the epoch of the closest encounter for the nominal trajectory.

Figures 4.15 and 4.16 display the results obtained by a DA-based Monte

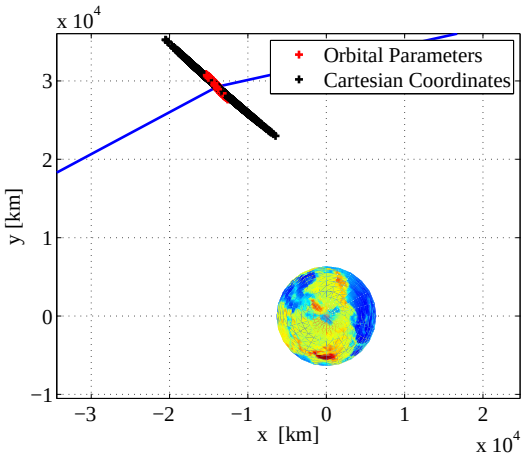

Figure 4.14: Apophis close encounter details.

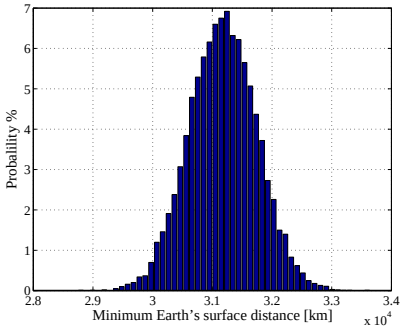

Figure 4.15: CED Monte Carlo analysis: uncertainty on orbital parameters.

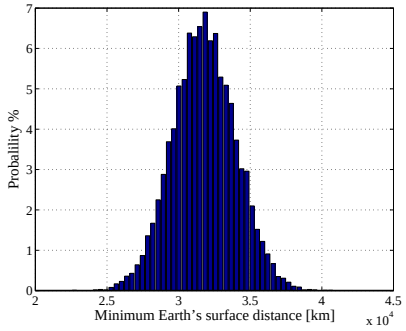

Figure 4.16: CED Monte Carlo analysis: uncertainty on cartesian coordinates.

Carlo simulation of 10000 virtual asteroids. The simulation based on uncertainties on orbital parameters returns a mean CED of 31781.9 km and a standard deviation of 568.7 km. The simulation based on cartesian coordinates gives almost the same mean value (31783.4 km) with a standard deviation of 2198.2, which is roughly four times bigger.

It has to be remarked that it would be interesting to investigate the possibility of using the high order Taylor expansion of the flow of ODE to directly propagate the Gaussian statistics as already shown for simpler dynamical models by Park and Scheeres [28]. Furthemore, note that the statistical analysis performed in this section utilizes the epoch of the close encounter of the nominal solution for the computation the CED of all the virtual asteroids. This issue is successfully addressed in the next section.

4.3 Minimum Distance Epoch Algorithm

As highlighted by Milani et al. [3], monitoring the close approaches by studying the nominal initial condition is not enough, as impact solutions can occur for different initial conditions, at a time when the nominal position is very far from the Earth. Referring to the techniques introduced in this work, evaluating the Taylor expansion of the flow at the epoch of the CED of the nominal solution is not appropriate, as each virtual asteroid belonging to the set of possible initial conditions has a different close encounter epoch.

A DA-based algorithm is introduced to reduce the computation of the minimum distance from the Earth, as well as the epoch of the close encounter, to the simple evaluation of polynomials for each virtual asteroid initial condition. Being at the basis of the algorithm, a technique is illustrated in Section 4.3.1 to obtain the arbitrary order Taylor expansion of the flow of ODE with respect to the final time. Then, the algorithm for the computation of the CED is presented in Section 4.3.2. Finally, the range of minimum distances for Apophis is estimated in Section 4.3.3 together with the techniques to identify the virtual asteroid with the closest approach.

4.3.1 High Order Expansion in Time of the Flow

The algorithm for the computation of the CED relies on the availability of the Taylor expansion of the flow of the ODE with respect to the final integration time. To this purpose, consider the ODE system

$$\frac{\mathrm{d}\boldsymbol{x}}{\mathrm{d}t} = \boldsymbol{f}(\boldsymbol{x}, t) \tag{4.4}$$

to be integrated from $t = t_0$ to $t = t_f$. Suppose the Taylor expansion of the flow with respect to t_f is of interest. We first shift the starting time by introducing the variable

$$\tilde{t} = t - t_0. \tag{4.5}$$

Using the variable $\tilde{t}$, equation (4.4) reads

$$\frac{\mathrm{d}\boldsymbol{x}}{\mathrm{d}\tilde{t}} = \boldsymbol{f}(\boldsymbol{x}, \tilde{t} + t_0), \tag{4.6}$$

and it must be integrate from $\tilde{t} = 0$ to $\tilde{t} = t_f - t_0$. Then, we introduce the variable

$$\tau = \frac{\tilde{t}}{t_f - t_0}. \tag{4.7}$$

Consequently,

$$\mathrm{d}\tilde{t} = (t_f - t_0)\,\mathrm{d}\tau \tag{4.8}$$

and equation (4.6) now reads

$$\frac{\mathrm{d}\boldsymbol{x}}{\mathrm{d}\tau} = (t_f - t_0) \cdot \boldsymbol{f}(\boldsymbol{x}, t_0 + (t_f - t_0)\tau), \tag{4.9}$$

that must be integrated from $\tau = 0$ to $\tau = 1$. Integrating equation (4.9) from $\tau = 0$ to $\tau = 1$ is equivalent to integrate the original ODE (4.4) from $t = t_0$ to $t = t_f$. However, a major advantage can be highlighted: the final time t_f, as well as the initial time t_0, have been moved from the integration interval to the ODE right hand side, where they appear as parameters. This allows the flow of the ODE to be expanded by means of the DA-based RKF78 integrator introduced in Section 4.1. More specifically, the final time t_f can be initialized as a DA variable:

$$[t_f] = {t_f}^0 + \delta t_f \tag{4.10}$$

in which ${t_f}^0$ is the reference final epoch. Then, equation (4.9) is integrated from $\tau = 0$ to $\tau = 1$ using the RKF78 integration scheme. By carrying out all the algebraic operations involved in the integration scheme in the DA framework allows the dependence of the solution on δt_f to be carried forward all throughout the integration. The result at time $\tau = 1$ is

$$\boldsymbol{x}_f = \mathcal{M}_{\boldsymbol{x}_f}(\delta t_f); \tag{4.11}$$

i.e., the Taylor expansion of the final solution with respect to the final time t_f. Note that the Taylor expansion of the solution with respect to the initial time can be similarly obtained by initializing t_0 as a DA variable.

The previous technique can be immediately applied to the integration of Apophis' motion in order to obtain the Taylor expansion of the final position and velocity with respect to the final epoch. In order to show the performances of the algorithm, set the initial condition $\boldsymbol{x}_0$ to be the nominal Apophis's position and velocity at the initial epoch t_0, and choose the reference epoch ${t_f}^0$ to be the epoch of the close encounter for the nominal Apophis' initial condition. The DA-based RKF78 scheme is then used to expand the solution of the ODE governing the asteroid's motion with respect to t_f. Figure 4.17 compares the nominal Apophis' distance from the Earth obtained through a pointwise integration with that computed by evaluating the Taylor expansion of Apophis' position with respect to t_f, in the interval ${t_f}^0 - 0.1\,\mathrm{days} < t_f < {t_f}^0 + 0.1\,\mathrm{days}$. More specifically, the results corresponding to three different expansion orders are illustrated. As it can be seen,

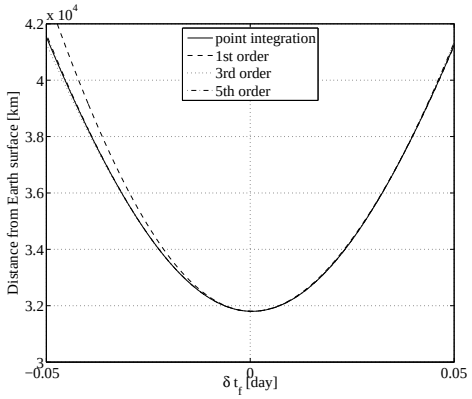

Figure 4.17: Apophis' distance from Earth's surface: comparison between the pointwise integration and the Taylor expansion of the flow with respect to the final integration epoch.

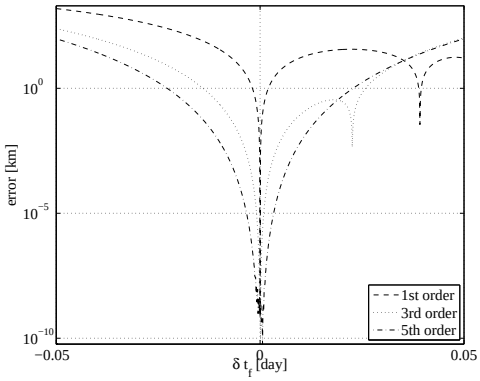

Figure 4.18: Apophis' distance from Earth's surface: analysis of the error of the Taylor expansion of the flow with respect to the final integration epoch.

the accuracy of the Taylor representation of the solution increases with the expansion order.

The accuracy of the Taylor representations is better assessed in Figure 4.18. In particular, the absolute difference between the result of the pointwise integration and Taylor expansion evaluation is plotted. As expected, the error is maximum at the boundary of the interval, whereas it tends to decrease toward the center; i.e., toward the reference epoch of the Taylor expansions.

The previous error analysis assumes the pointwise integration as the reference solution. However, based on the analysis of the accuracy of the RKF78-based integration presented in Chapter 3, the error of the pointwise integration shows a steep increase in the region immediately following the pericenter of the orbit. This must be deemed as the main contribution to the behavior of the error of the Taylor expansion after the reference epoch.

Note that a third order Taylor expansion of the solution assures a maximum error at $|\delta t_f| = 10^{-4}$ days of the order of 10^{-8} km. For this reason, the results presented in the followings will refer to third order Taylor expansions.

4.3.2 Algorithm

The algorithm for the computation of the CED of each virtual asteroid belonging to the initial set is presented in this section. The main rationale behind this algorithm comes from the observation that both the CED and the associated epoch differ for each virtual asteroid belonging to the initial set.

Consequently, the motion of each virtual asteroid should be integrated separately to fully characterize its close encounter. However the major drawback of this approach is the need for multiple computationally intensive pointwise integrations of the dynamics.

having an explicit algebraic formula for the solution of the previous problem would be particularly helpful in practical applications as for any virtual asteroid a simple function evaluation would suffice to obtain both the CED and the corresponding epoch. DA techniques can effectively serve this purpose by providing the desired explicit relation in terms of Taylor polynomials.

To this aim, suppose the close approach of the nominal asteroid has been identified to occur at the epoch t_f^0, and consider the integration of the asteroid dynamics

$$\frac{\mathrm{d}\boldsymbol{x}}{\mathrm{d}t} = \boldsymbol{f}(\boldsymbol{x}, t), \tag{4.12}$$

from $t = t_i$ to $t = t_f^0$. Initialize the initial state and the final integration epoch as DA variables; i.e.,

$$\begin{aligned} [\boldsymbol{x}_i] &= \boldsymbol{x}_i^0 + \delta\boldsymbol{x}_i \\ [t_f] &= t_f^0 + \delta t_f, \end{aligned} \tag{4.13}$$

where $\boldsymbol{x}_i^0$ is the initial condition corresponding to the nominal asteroid. Using the DA-based RKF78 integrator and the technique introduced in Section 4.3.1, flow the initial condition under (4.12) to obtain the map

$$\boldsymbol{x}_f = \boldsymbol{x}_f^0 + \delta\boldsymbol{x}_f = \mathcal{M}_{\boldsymbol{x}_f}(\delta\boldsymbol{x}_i, \delta t_f). \tag{4.14}$$

The map (4.14) is the n-th order Taylor expansion of the flow of (4.12) with respect to $\boldsymbol{x}_i$ and δt_f, about the nominal initial condition $\boldsymbol{x}_i^0$ and the nominal close encounter epoch t_f^0. Based on a mere DA-based computation, the final solution $\boldsymbol{x}_f$ can be used to compute the distance from the Earth

$$d_f = d_f^0 + \delta d_f = \mathcal{M}_{d_f}(\delta\boldsymbol{x}_i, \delta t_f). \tag{4.15}$$

More specifically, map (4.15) is the Taylor expansion of the asteroid distance from the Earth with respect to $\boldsymbol{x}_i$ and δt_f; i.e., it describes how the distance varies depending on the virtual asteroid and the final integration epoch.

Using the derivation operator available in the DA framework, the derivative $d'_f = \mathrm{d}(d_f)/\mathrm{d}t_f$ can be obtained as a Taylor expansion

$$d'_f = {d'_f}^0 + \delta d'_f = \mathcal{M}_{d'_f}(\delta\boldsymbol{x}_i, \delta t_f). \tag{4.16}$$

The constant part of the map (4.16), ${d'_f}^0$, is the derivative of the distance from the Earth of the nominal solution at its close encounter; i.e., at CED epoch. Consequently, this is a stationary point for the nominal solution, and ${d'_f}^0 = 0$. Then, the map (4.16) reduces to

$$\delta d'_f = \mathcal{M}_{d'_f}(\delta \boldsymbol{x}_i, \delta t_f). \tag{4.17}$$

Consider the map

$$\begin{pmatrix} \delta d'_f \\ \delta \boldsymbol{x}_i \end{pmatrix} = \begin{pmatrix} \mathcal{M}_{d'_f} \\ \mathcal{I}_{\boldsymbol{x}_i} \end{pmatrix} \begin{pmatrix} \delta \boldsymbol{x}_i \\ \delta t_f \end{pmatrix}, \tag{4.18}$$

which is built by concatenating $\mathcal{M}_{d'_f}$ with the identity map for δt_f. Map (4.18) can now be inverted to obtain

$$\begin{pmatrix} \delta \boldsymbol{x}_i \\ \delta t_f \end{pmatrix} = \begin{pmatrix} \mathcal{M}_{d'_f} \\ \mathcal{I}_{\boldsymbol{x}_i} \end{pmatrix}^{-1} \begin{pmatrix} \delta d'_f \\ \delta \boldsymbol{x}_i \end{pmatrix}. \tag{4.19}$$

Then, concatenate map (4.15) to the identity map for δt_f to obtain

$$\begin{pmatrix} d_f \\ \delta t_f \end{pmatrix} = \begin{pmatrix} \mathcal{M}_{d_f} \\ \mathcal{I}_{t_f} \end{pmatrix} \begin{pmatrix} \delta \boldsymbol{x}_i \\ \delta t_f \end{pmatrix}. \tag{4.20}$$

Map (4.20) can now be composed with map (4.19) to obtain

$$\begin{pmatrix} d_f \\ \delta t_f \end{pmatrix} = \begin{pmatrix} \mathcal{M}_{d_f} \\ \mathcal{I}_{t_f} \end{pmatrix} \circ \begin{pmatrix} \mathcal{M}_{d'_f} \\ \mathcal{I}_{\boldsymbol{x}_i} \end{pmatrix}^{-1} \begin{pmatrix} \delta d'_f \\ \delta \boldsymbol{x}_i \end{pmatrix}, \tag{4.21}$$

which relates the final distance and the variation of the final epoch to the displacement of the derivative of the final distance ($\delta d'_f$) from its nominal value (${d'_f}^0 = 0$) and the displacement of the virtual asteroid from the nominal one in terms of initial state ($\delta \boldsymbol{x}_i$). The necessary condition for CED computation is

$$d'_f = 0. \tag{4.22}$$

As the reference value ${d'_f}^0 = 0$, the condition (4.22) translates into $\delta d'_f = 0$. Substituting into (4.21) yields

$$\begin{pmatrix} {d_f}^* \\ {\delta t_f}^* \end{pmatrix} = \begin{pmatrix} \mathcal{M}_{d_f} \\ \mathcal{I}_{t_f} \end{pmatrix} \circ \begin{pmatrix} \mathcal{M}_{d'_f} \\ \mathcal{I}_{\boldsymbol{x}_i} \end{pmatrix}^{-1} \begin{pmatrix} 0 \\ \delta \boldsymbol{x}_i \end{pmatrix}. \tag{4.23}$$

Eventually, map (4.23) delivers the desired explicit relation between the CED (${d_f}^*$) and the epoch at which it is reached ($t_f^0 + \delta {t_f}^*$), and the displacement

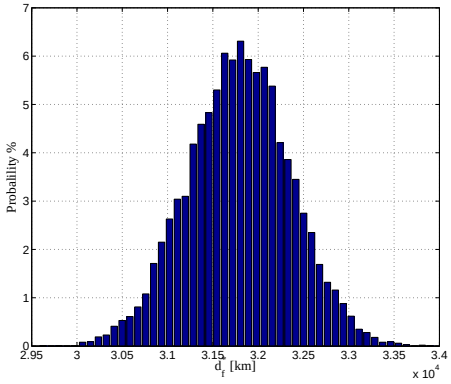

Figure 4.19: Monte Carlo analysis of virtual asteroids CED.

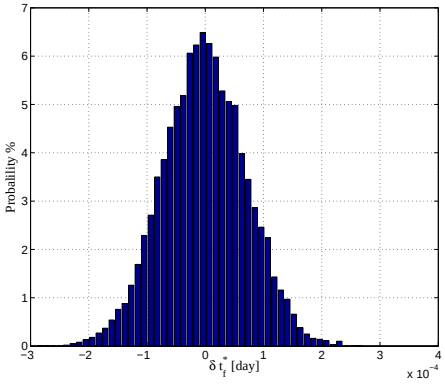

Figure 4.20: Monte Carlo analysis of virtual asteroids CED epochs.

of the initial condition from the nominal value ($\delta \boldsymbol{x}_i$), in terms of Taylor polynomials. More in detail, given any virtual asteroid belonging to the initial set (which corresponds to a specific value of the displacement $\delta \boldsymbol{x}_i$), the simple evaluation of the polynomials in(4.23) delivers the CED and the epoch at which it is reached.

The application of the previous algorithm to the analysis of Apophis' close encounter is presented in the followings. To this aim, a Monte Carlo simulation is performed, based on the uncertainties on the orbital parameters. More specifically, 10000 virtual asteroids are generated with a normal random distribution, with mean values and deviations taken from Table 4.1. For each sample, the displacement with respect to the nominal initial conditions is computed and map (4.23) is evaluated to obtain the CED and the associated close encounter epoch. The result is reported in Figure 4.19 in terms of probability distribution for ${d_f}^*$. The analysis of the results shows that the mean CED is 3.18024×10^4. This result is comparable to the one shown in FIgure 4.15, underling that for Apophis' test case all the virtual asteroids have a common CED epoch.

For the same virtual asteroids, map (4.23) is also evaluated to obtain the epochs at wich the CED are attained. The result is presented in Figure 4.20 in terms of the probability distribution of the displacement $\delta {t_f}^*$ from the nominal epoch t_f^0. As it can be seen, the maximum displacement is of the order of 2×10^{-4} day. As stated in Section 4.3.1, this is compatible with an accuracy of the Taylor expansion with respect to the final epoch of the order of 10^{-8} km, which is deemed acceptable for the close encounter characterization.

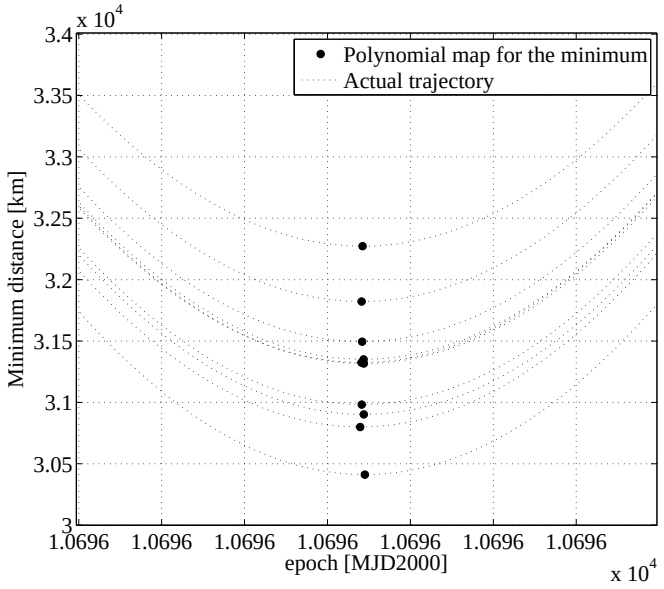

Figure 4.21: Accuracy of the CED algorithm: virtual asteroids actual trajectories.

For the sake of completeness, an accuracy analysis of the results is presented in Figure 4.21. Ten virtual asteroids are randomly selected from the initial set. For each virtual asteroid, the minimum distance and the corresponding epoch are reported in figure. Then, a pointwise integration of the motion of each asteroid is performed to obtain their trajectories in Earth's sphere of influence. The resulting distance from Earth's surface is plotted in Figure 4.21. Although the accuracy on the identification of the epoch of the close encounter is not clearly visualized in figure, due to the very small displacement in ${t_f}^*$, Figure 4.21 clearly shows that the algorithm is able to accurately identify CED values of the resulting trajectories.

4.3.3 Range of CED

In this section, the polynomial representation of the CED is exploited to calculate both its range and its minimum value. This result can be straightforwardly used to evaluate the possibility of an Earth's impact occurrence.

An the estimate of the minimum CED could be identified by bounding the range of the polynomial map (4.23) over the whole set of possible initial conditions. Estimating the actual range of a multivariate arbitrary order polynomial over given domains is not an easy task. This precludes the possibility of assessing the exact range $[{d_f}^*_{\min}, {d_f}^*_{\max}]$ of the polynomial for ${d_f}^*$

in general. Nevertheless, an accurate enclosure $[\underline{d_f}^*, \overline{d_f}^*]$ of the exact range, with $\underline{d_f}^*$ and $\overline{d_f}^*$ different from but close to ${d_f}^*_{\min}$ and ${d_f}^*_{\max}$ respectively could suffice for the characterization of the close encounter.

Moreover, if the available enclosure is also validated (i.e., if $[{d_f}^*_{\min}, {d_f}^*_{\max}] \subset [\underline{d_f}^*, \overline{d_f}^*]$), then it could be used to discard impact's occurrence. More specifically, being the enclosure validated, if $\underline{d_f}^* > 0$, then the polynomial for ${d_f}^*$ is demonstrated to be strictly positive. Consequently, assuming that the polynomial map (4.23) is sufficiently accurate to represent ${d_f}^*$ for the entire set of initial conditions, this information could be used to entail that the minimum CED is strictly positive; i.e., the probability of an impact's occurrence is zero.

To obtain such a validated enclosure, the linear dominated bounder (LDB) algorithm is used to estimate the range of ${d_f}^*$. The LDB algorithm is introduced in the framework of Taylor models and it is based on the observation that the dominating part of the total bounds of a polynomial are expected to come from the linear part (see [5] for details). This algorithm is capable of producing validated bounds for arbitrary order Taylor models. However, it can be used to get validated bounds of an arbitrary order Taylor polynomial by transforming into a Taylor model. The LDB algorithm is then used on the resulting Taylor model to get validated estimates of the range of the polynomial.

Figure 4.22 illustrates the results of the application of the LDB algorithm to the polynomial map (4.23) for ${d_f}^*$. The CED and the CED epochs corresponding to the 10000 virtual asteroids of the Monte Carlo simulation performed in Section 4.3.2 are reported. The lower and upper bounds, obtained by applying the LDB algorithm to ${d_f}^*$ over the set of initial conditions defined in Table 4.1, are plotted. The lower bound is strictly positive and equal to 28545.8 km. As the LDB bounds are validated, the range of the polynomial for ${d_f}^*$ over the considered set of initial conditions is demonstrated to be strictly positive. Consequently, assuming the polynomial map is sufficiently accurate, the probability of an impact occurrence is zero. The analysis of Figure 4.22 could raise doubts about the accuracy of the LDB bounds. In particular, the LDB bounds seems to largely overestimate the cloud of the Monte Carlo simulation. However, it must be noticed that the LDB algorithm computes the bounds of the polynomial over an interval box on its variables. Consequently, the bounds take account of the edges of the interval box, which can significantly contribute to the identification of the actual range of the polynomial. These regions are usually missed by the statistical distributions used in the Monte Carlo simulation, due to the different uncertainty modeling and treatment. For this reason, it is helpful to identify

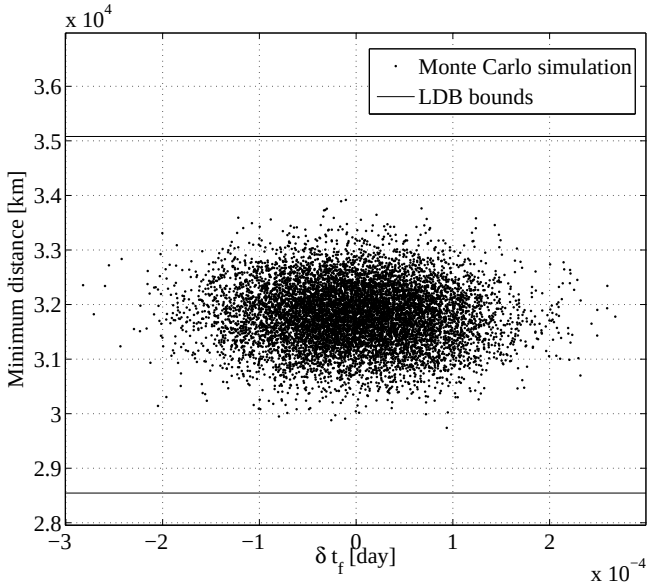

Figure 4.22: CED bounds obtained using LDB.

an initial condition with a CED equal to the lower bound identified by the LDB algorithm. The benefit of this analysis would be twofold:

- the accuracy of the LDB algorithm in the identification of the minimum of the CED would be assessed;
- the analysis would lead to the identification of the most dangerous initial condition.

To this aim, an optimization algorithm is run to find the minimum ${d_f}^*$. More specifically, the objective function to be minimized is the polynomial for ${d_f}^*$, the optimization variables are its variables (i.e., the orbital parameters identifying the initial conditions), whereas the search space is limited to the set of possible initial conditions defined in Table 4.1.

It is worth noticing that this approach is very similar to the general and emerging technique of assisting the uncertainty analysis by means of optimization tools [31]. The basic idea is trying to find the possible range of a performance index by minimizing and maximizing its values, acting on the uncertain parameters. The minimization and maximization processes are performed by means of optimization tools: the performance index is the objective function, whereas the optimization variables are the uncertain parameters that vary within their uncertainty range. This technique could be readily used to identify the smallest possible distance of Apophis during

Table 4.3: Initial condition corresponding to the closest approach obtained by the SQP optimization process. Note: a_i^0, e_i^0, i_i^0, Ω_i^0, ω_i^0, E_i^0 denote the nominal initial condition.

Parameter	Value	
${a_i}^*$	$a_i^0 - 3\,\sigma = 0.936366882199485$	AU
${e_i}^*$	$e_i^0 - 3\,\sigma = 0.193687423932093$	–
${i_i}^*$	$i_i^0 - 3\,\sigma = 0.057810319285634$	rad
${\Omega_i}^*$	$\Omega_i^0 + 3\,\sigma = 3.566854704892561$	rad
${\omega_i}^*$	$\omega_i^0 + 3\,\sigma = 2.250095563949659$	rad
${E_i}^*$	$E_i^0 + 3\,\sigma = 1.790310103310970$	rad
$\min {d_f}^*$	28545.82920848911	km

its close encounter: for each initial condition belonging to the initial set, the objective function would be defined as the minimum distance from Earth of the resulting trajectory. However, in a straightforward application of this technique, each computation of the minimum distance from Earth would involve the integration of the asteroid's motion till its close encounter with Earth. Within an optimization process, this could make the computational burden prohibitive, as each objective function evaluation would involve an integration process. The advantage of using DA techniques is then evident. As stated above, for each initial condition the integration process to compute the minimum distance from Earth is substituted by the fast evaluation of the polynomial map for ${d_f}^*$. Consequently, each objective function evaluation only involves the evaluation of a polynomial. This significantly decreases the computational burden of the optimization process. In this way, DA techniques can improve the performances of the uncertainty and parametric analysis tools based on optimization processes.

A local optimization algorithm based on sequential quadratic programming (SQP) is used in a first istance. Local optimization algorithms need a first guess solution to be supplied by the user. The nominal initial condition (i.e., the center of the search space) is selected to this purpose. The SQP-based local optimizer implemented in the Matlab built-in function "fmincon" is used. The result of the optimization process is reported in Table 4.3, whereas the minimum distance and its occurrence epoch corresponding to the identified solution, which are obtained by evaluating the map (4.23), are illustrated in Figure 4.23. The identified minimum CED is $6.4 \cdot 10^{-9}$ km above the validated lower bound $\underline{{d_f}^*}$. Consequently, the LDB algorithm's

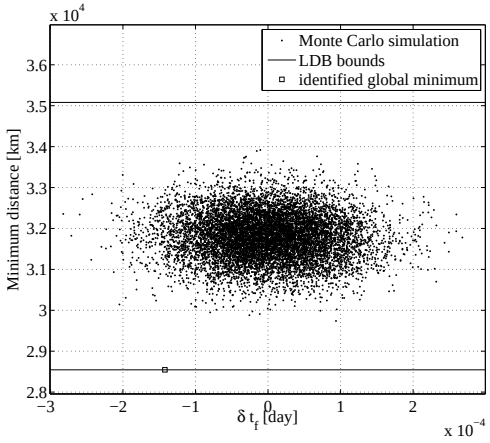

Figure 4.23: Closest CED approach obtained using a SQP local optimization process.

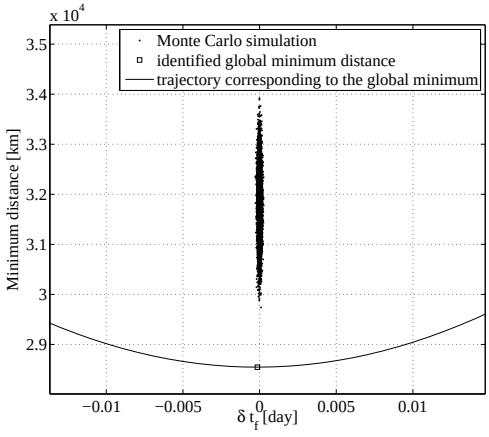

Figure 4.24: Actual trajectory corresponding to the identified closest approach.

accuracy is demonstrated.

Note that the solution reported in Table 4.3 is located on a box vertex. This is highlighted in the table as the values for ${a_i}^*$, ${e_i}^*$, and ${i_i}^*$ are the minimum allowed for a_i, e_i, and i_i, respectively, whereas the values for ${\Omega_i}^*$, ${\omega_i}^*$, ${E_i}^*$ are the maximum allowed for Ω_i, ω_i, E_i. The distance from Earth's surface during the entire Earth's close encounter corresponding to the initial condition reported in Table 4.3 is plotted in Figure 4.24. The figure highlights the good accuracy of the map (4.23) for initial conditions lying on a vertex of the initial box (i.e., far from the reference point of the Taylor expansions).

One of the major drawbacks of the local optimizers is that they tend to converge to a minimum close to the first guess solution. Consequently, they tend to get stuck in local minimum. Moreover, only one minimum is identified during the optimization process. In case two global minima exist corresponding to two different solutions of the search space, only one of them can be identified by a single local optimization run. The use of the validated global optimizer COSY-GO [30] is proposed to deal with the previous issues. By exploiting the capability of Taylor models of delivering the validated enclosure of functions, this optimizer returns the mathematically proven enclosure of the global minimum of a function over a given search space. Moreover, being based on a branch and bound scheme, if more than one global minimum exists, COSY-GO is able to keep track of all of them, delivering validated enclosures of all the global minima.

As in the case of the SQP optimizer, COSY-GO was used to find the

Table 4.4: Enclosure of the initial condition corresponding to the closest approach obtained by COSY-GO.

Parameter	Validated enclosure	
$a_i{}^*$	$[0.936366882199484,\ 0.936366882199485]$	AU
$e_i{}^*$	$[0.193687423932091,\ 0.193687423932101]$	–
$i_i{}^*$	$[0.057810319285633,\ 0.057810319285710]$	rad
$\Omega_i{}^*$	$[3.566854704892544,\ 3.566854704892616]$	rad
$\omega_i{}^*$	$[2.250095563949643,\ 2.250095563949715]$	rad
$E_i{}^*$	$[1.790310103310950,\ 1.790310103310999]$	rad
$\min d_f{}^*$	$[28545.82920845387, 28545.82920850764]$	km

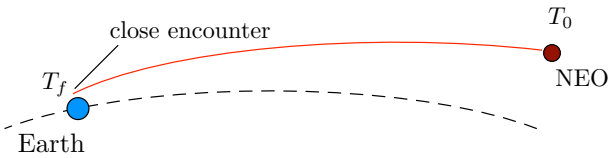

Figure 4.25: At the measurement epoch t_0, a close encounter has been identified to occur at epoch t_f.

global minimum of the polynomial for $d_f{}^*$ over the set of possible initial conditions. The optimization process takes 0.12 s on a 2GHz Intel Core Duo MacBook running MacOSX. At the end of the optimization process, only one solution is delivered. This demonstrates that only one global minimum exist. The enclosure of the global minimum is reported in Table 4.4. The interval enclosures reported in Table 4.4 sharply enclose the solution reported in Table 4.3. This demonstrates that the solution obtained by means of the local optimizer can be considered as the global minimum, and it can be considered as the solution corresponding to the closest approach to Earth.

4.4 Impact Leading Condition Algorithm

Section 4.3.2 has introduced an algorithm for the identification of CED and its occurrence epoch for each initial condition belonging to the initial set. This has been shown to be instrumental for the characterization of the close encounter and the verification of possible impacts. Suppose that the occurrence of a hazarous close encounter has been identified to occur at epoch t_f based on the measurements available at epoch t_0. Suppose that a further

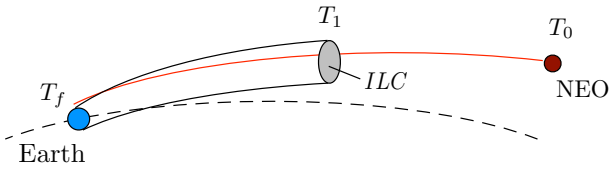

Figure 4.26: Given a further measurement epoch t_1, the ILC are sought, which can be used to check the impact occurrence based on the measurements at t_1.

measurement of the asteroid state is scheduled for epoch t_1 (see Figure 4.25). The availability of information about the conditions the asteroid state must satisfy at t_1 to impact the Earth at t_f could be used by any astronomer to get immediate confirmation on the occurrence of an impact. This conditions are referred to as impact-leading conditions (ILC) in this work (see Figure 4.26). More specifically, once the measurement of the asteroid state at time t_1 is available, its compliance with the ILC could be checked and the impact occurrence could be verified.

An algorithm for the identification of the ILC is presented in this section, based on the use of DA techniques. It can be viewed as a step that immediately follows the identification of the map (4.23) for CED. Suppose the ILC for the measurement epoch t_i are to be identified. Given the nominal initial conditions and the uncertainty set, the CED algorithm can be applied to obtain the map (4.23). Extract the first component of the map, which will be indicated as

$$d_f{}^* = \mathcal{M}_{d_f{}^*}(\delta \boldsymbol{x}_i). \tag{4.24}$$

The ILC can be identified by imposing that $d_f{}^* \leq 0$. Within this work, the equality condition $d_f{}^* = 0$ will be analyzed. Some hints on how to impose the inequality constraint $d_f{}^* \leq 0$ will be given at the end of the section.

A constraint manifold in the set of initial conditions is associated to the constraint $d_f{}^* = 0$. More specifically, one state variable $x_{i,k}$ could be expressed as a function of the remaining five state variables $x_{i,j\neq k}$; i.e.,

$$x_{i,k} = f(x_{i,j\neq k}). \tag{4.25}$$

In this way, given a set of possible values for $x_{i,j\neq k}$, the associated values of $x_{i,k}$ that would bring to a minimum distance from Earth's surface equal to zero can be assessed. Identifying the relation (4.25) is not easy, as it requires analytical information that are not available in the case of classical pointwise integrations, or that are not sufficiently accurate in the case of techniques based on linear assumptions. The use of DA techniques is proposed here as

a tool to obtain the explicit relation (4.25) in terms of an arbitrary order Taylor expansion. To this aim, suppose the polynomial (4.24) has been already identified and consider the following map:

$$\begin{pmatrix} {d_f}^* \\ \delta \boldsymbol{x}_{i,j\neq k} \end{pmatrix} = \begin{pmatrix} \mathcal{M}_{{d_f}^*} \\ \mathcal{I}_{\boldsymbol{x}_{i,j\neq k}} \end{pmatrix} (\delta \boldsymbol{x}_i) = \begin{pmatrix} \mathcal{M}_{{d_f}^*} \\ \mathcal{I}_{\boldsymbol{x}_{i,j\neq k}} \end{pmatrix} \begin{pmatrix} \delta x_{i,k} \\ \delta \boldsymbol{x}_{i,j\neq k} \end{pmatrix}. \tag{4.26}$$

Map (4.26) can be inverted to obtain

$$\begin{pmatrix} \delta x_{i,k} \\ \delta \boldsymbol{x}_{i,j\neq k} \end{pmatrix} = \begin{pmatrix} \mathcal{M}_{{d_f}^*} \\ \mathcal{I}_{\boldsymbol{x}_{i,j\neq k}} \end{pmatrix}^{-1} \begin{pmatrix} {d_f}^* \\ \delta \boldsymbol{x}_{i,j\neq k} \end{pmatrix}. \tag{4.27}$$

The constraint ${d_f}^* = 0$ can now be imposed in the map (4.27):

$$\begin{pmatrix} \delta x_{i,k} \\ \delta \boldsymbol{x}_{i,j\neq k} \end{pmatrix} = \begin{pmatrix} \mathcal{M}_{{d_f}^*} \\ \mathcal{I}_{\boldsymbol{x}_{i,j\neq k}} \end{pmatrix}^{-1} \begin{pmatrix} 0 \\ \delta \boldsymbol{x}_{i,j\neq k} \end{pmatrix}. \tag{4.28}$$

The first component of the map (4.28) can be extracted, which will be indicated as

$$\delta x_{i,k} = \mathcal{M}_{{d_f}^*=0} (\delta \boldsymbol{x}_{i,j\neq k}). \tag{4.29}$$

Map (4.29) is the arbitrary order Taylor expansion of the explicit relation (4.25) about the reference nominal values $\boldsymbol{x}^0_{i,j\neq k}$ of five components of the initial state vector. More specifically, for each initial condition, the displacement $\delta \boldsymbol{x}_{i,j\neq k}$ of $\boldsymbol{x}_{i,j\neq k}$ from its nominal value $\boldsymbol{x}^0_{i,j\neq k}$ can be computed. Then, the map (4.29) is evaluated to obtain the correction $\delta x_{i,k}$ to the nominal value $x^0_{i,k}$ of $x_{i,k}$ that would make the asteroid impact the Earth. In other words, the trajectory identified by

$$\begin{aligned} x_{i,k} &= x^0_{i,k} + \delta x_{i,k} \\ \boldsymbol{x}_{i,j\neq k} &= \boldsymbol{x}^0_{i,j\neq k} + \delta \boldsymbol{x}_{i,j\neq k} \end{aligned} \tag{4.30}$$

has a minimum distance from Earth equal to zero. As the polynomial (4.29) is a Taylor expansion of the constraint manifold (4.25), the accuracy on the satisfaction of the constraint ${d_f}^* = 0$ depends on the order of the Taylor expansion and the displacement $\delta \boldsymbol{x}_{i,j\neq k}$. It is worth mentioning that, once $\delta x_{i,k}$ has been computed from (4.29), the new displacement vector $\delta \boldsymbol{x}_i = (\delta x_{i,k}, \delta \boldsymbol{x}_{i,j\neq k})$ can be set up and the map (4.23) can be evaluated to obtain the new epoch at which the minimum distance is reached.

The algorithm is applied to the Apophis in the followings. Similarly to Section 4.3.2, the state vector is defined by the set of six orbital parameters $(a, e, i, \Omega, \omega, E)$, and the CED algorithm is used to obtain the map (4.24).

As the resulting map is meant to be used to represent regions where ${d_f}^*$ is close to zero, these being far from the nominal value for ${d_f}^*$, 6-th order computations are used. Then, the ILC algorithm described above is applied to expand the constraint manifold as in equation (4.29). More specifically, $x_{i,k}$ is selected to be the initial value of the semi-major axis of Apophis' orbit, whereas $\boldsymbol{x}_{i,j\neq k}$ is made up by the remaining orbital parameters; i.e.,

$$\begin{aligned} x_{i,k} &= a_i \\ \boldsymbol{x}_{i,j\neq k} &= (e_i, i_i, \Omega_i, \omega_i, E_i). \end{aligned}$$

and the map (4.29) becomes

$$\delta a_i = \mathcal{M}_{{d_f}^*=0}\left(\delta e_i, \delta i_i, \delta\Omega_i, \delta\omega_i, \delta E_i\right). \tag{4.31}$$

For each initial condition, the displacement $(\delta e_i, \delta i_i, \delta\Omega_i, \delta\omega_i, \delta E_i)$ is computed and the 6-th order map (4.31) is evaluated to obtain the value the semi-major axis must have to satisfy ${d_f}^* = 0$. It is worth mentioning that the selection of $x_{i,k} = a_i$ is not based on any rationale: a different selection could have been considered and future work will address the problem of identifying the most suitable choice.

The algorithm is applied to the nominal initial condition. The initial value the semi-major axis must have to satisfy ${d_f}^* = 0$ in case the remaining orbital parameters assume their nominal value is computed. To this aim, the polynomial (4.31) is evaluated at $(\delta e_i, \delta i_i, \delta\Omega_i, \delta\omega_i, \delta E_i) = (0, 0, 0, 0, 0)$. The resulting trajectory is integrated and Apophis' distance from Earth's surface is plotted in Figure 4.27, where it is compared with the distance corresponding to the nominal initial condition. As it can be seen, the new trajectory is significantly closer to Earth's surface than the nominal one, tending to satisfy the constraint ${d_f}^* = 0$ and the impact occurrence. However, a closer look to the new CED (see Figure 4.28) reveals an accuracy problem. The new minimum distance is of the order of 700 km; i.e., the error on the satisfaction of ${d_f}^* = 0$ is of the order of 10^3 km. This means that map (4.23) used in the ILC algorithm to represent ${d_f}^*$ has an accuracy of 10^3 km for the computed value of δa_i. In Figure 4.28 this feature is highlighted by the square, which represents the point $({d_f}^*, {t_f}^*)$ obtained from map (4.23). The difference between the computed value of ${d_f}^*$ and the actual CED is of the order of 10^3 km.

The first attempt to overcome the previous accuracy problem consisted in increasing the order of the Taylor expansions, but no significant improvement was achieved. This is due to the fact that the Taylor expansions do not converge for the resulting value of δa_i. An alternative strategy is then pursued. A new initial condition $\tilde{\boldsymbol{x}}_i^0$ is set up by concatenating the obtained

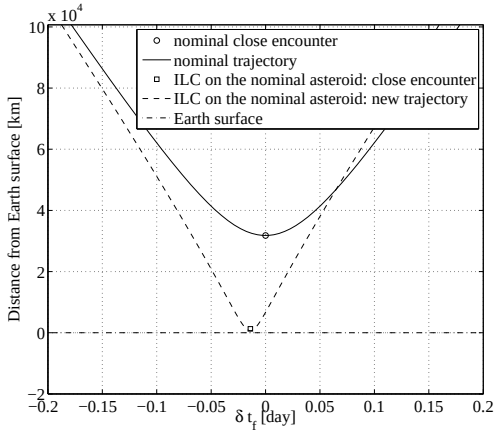

Figure 4.27: Comparison between the nominal close encounter and the close encounter generated by the ILC algorithm applied to the nominal initial conditions.

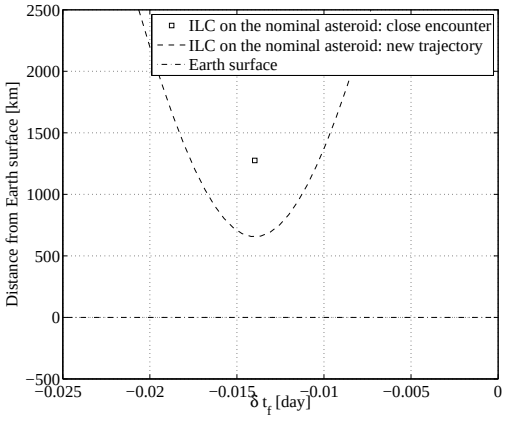

Figure 4.28: Details on the comparison between the nominal close encounter and the close encounter generated by the ILC algorithm applied to the nominal initial conditions.

value for a_i, $\tilde{a}_i^0 = a_i^0 + \delta a_i$, with the nominal initial values for the other orbital parameters:

$$\tilde{\boldsymbol{x}}_i^0 = (\tilde{a}_i^0, e_i^0, i_i^0, \Omega_i^0, \omega_i^0, E_i^0). \tag{4.32}$$

The new initial condition (4.32) is used as reference initial condition for a new application of the ILC algorithm. In this second iteration, a new 6-th order expansion of the flow of the ODE describing the asteroid's motion is computed at the minimum distance epoch ${t_f}^*$ obtained in the first iteration. Then, the CED algorithm is applied to obtain a new map for ${d_f}^*$ and ${t_f}^*$. The ILC algorithm is then applied to compute a new explicit representation of the constraint manifold ${d_f}^* = 0$:

$$\delta\tilde{a}_i = \mathcal{M}_{{d_f}^*=0}\,(\delta e_i, \delta i_i, \delta\Omega_i, \delta\omega_i, \delta E_i). \tag{4.33}$$

The components of the vector $(\delta e_i, \delta i_i, \delta\Omega_i, \delta\omega_i, \delta E_i)$ still represent the displacement of $(e_i, i_i, \Omega_i, \omega_i, E_i)$ from the original reference value $(e_i^0, i_i^0, \Omega_i^0, \omega_i^0, E_i^0)$. On the other hand, $\delta\tilde{a}_i$ now represents the displacement of a_i from the new reference value $\tilde{a}_i^0$. Considering the relatively low error of the first application of the ILC algorithm, $\delta\tilde{a}_i$ is now supposed to assume significantly lower values than δa_i, so assuring a better accuracy to be achieved using 6-th order Taylor expansions. This is confirmed in Figures 4.29 and 4.30: the results of the first application of the ILC algorithm are compared with the new close

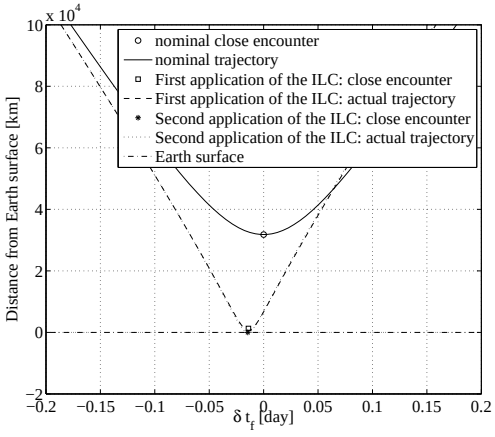

Figure 4.29: Comparison between the nominal close encounter and the close encounters generated by two applications of the ILC algorithm.

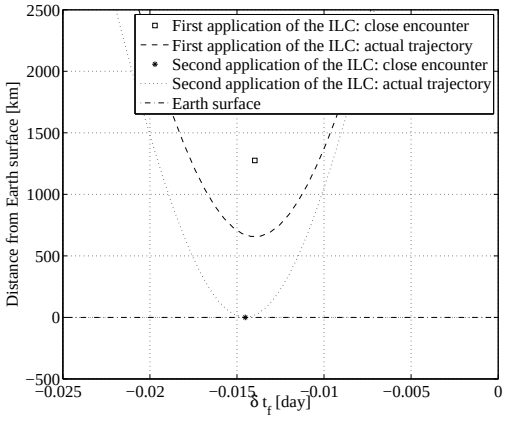

Figure 4.30: Details on the accuracy on the identification of the ILC: comparison between two successive application of the algorithm.

encounter obtained with the second application of the same algorithm. As Figure 4.30 shows, the accuracy on the satisfaction of the constraint ${d_f}^* = 0$ is significantly higher: the achieved CED is now of the order of 10^{-1} km.

The previous figures refer to the ILC for the nominal virtual asteroid. Nevertheless, the map (4.33) can be used to compute the impact-leading value of a_i for any displacement $(\delta e_i, \delta i_i, \delta\Omega_i, \delta\omega_i, \delta E_i)$. This is illustrated in Figures 4.31 and 4.32. The same ten random samples analyzed in Figure 4.21 are processed here. For each sample, the displacement $(\delta e_i, \delta i_i, \delta\Omega_i, \delta\omega_i, \delta E_i)$ is computed and the map (4.33) is evaluated to obtain the corresponding impact-leading values of a_i. The resulting trajectories are then integrated and the CED are plotted. Figure 4.32 show that all the trajectories accurately satisfy the impact condition ${d_f}^* = 0$.

Suppose now the measured asteroid state at the epoch of the computed ILC is available in terms of an uncertainty set. The LDB algorithm introduced in Section 4.3.3 can now be profitably used to bound the ILC. More specifically, given the uncertainty intervals on $(e_i, i_i, \Omega_i, \omega_i, E_i)$, the LDB algorithm can be used to get validated lower and upper bounds for the impact-leading values of a_i, by applying it to the polynomial in (4.33). For the particular case analyzed in the previous figures, the measured set of possible initial conditions is trivially represented by the nominal initial conditions and the $3\,\sigma$ values reported in Table 4.1. The resulting LDB-based validated

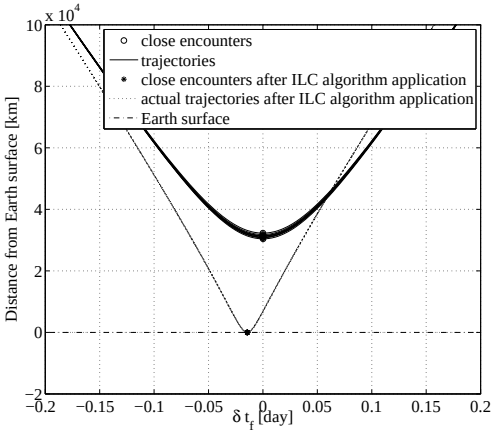

Figure 4.31: Application of the ILC algorithm to 10 random virtual asteroids.

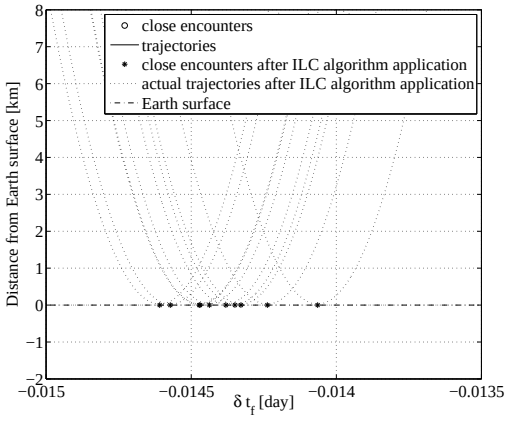

Figure 4.32: Details on the application of the ILC algorithm to 10 random virtual asteroids.

enclosure of the impact-leading conditions is

$$[\,\underline{a}_i^{ILC},\, \overline{a}_i^{ILC}\,] = [\,0.936363603705040,\, 0.936364034573461\,]. \tag{4.34}$$

The intersection between the measured interval on a_i reported in Table 4.1 and the validated interval in (4.34) is empty; i.e., no parts of the measured set lie into the set of ILC. This confirms that, based on the measured asteroid state, the occurrence of an impact with Earth is discarded.

The previous result seems obvious, as the ILC algorithm was applied to the epoch t_i, where the analyses performed in the previous sections have already discarded the impact's occurrence. However, the strength of the algorithm is that the ILC can be computed once for any planned measurement epoch. Being based on the arbitrary order expansion of the flow of the ODE, only good estimates of the nominal asteroid state at the planned measurement epochs are needed. These estimates are used as reference solutions for the Taylor expansions, and the ILC algorithm works straightforwardly once the expansion of the flow from the measurement epochs to the close encounter epoch is available. Similarly to before, once the asteroid state at the selected epochs is measured, the LDB algorithm can be used to immediately verify impact's occurrence without the need of running any further integration.

It is worth observing that all the previous results have been obtained by imposing ${d_f}^* = 0$. The algorithm can be generalized to impose the more general equality constraint ${d_f}^* = 0 + \delta d$, where a new DA variable d representing the depth is introduced. All the Taylor polynomials appearing in this

section would then include the expansion terms in d, and the ILC would be a function of the depth the asteroid will reach from Earth's surface. This generalization will allow the inequality ${d_f}^* \leq 0$ to be better managed in future works.

4.5 Analysis of Resonant Returns

This section deals with the analysis of possible resonant returns. In particular the possibility of a resonant return on April 13, 2036 is studied. This is referred to as 6:7 resonance in which the close encounter happens after 6 orbital periods of the asteroid and 7 of the Earth. The analysis is performed considering uncertainties on orbital parameters to limit the set of possible solutions after the first flyby. First of all the DA integration in the heliocentric reference frame is performed until the date of the possible second encounter, 13252.67623 MJD2000. Figure 4.33 and 4.34 show Apophis trajectory and integration error for the nominal solution, comparing the results with those of JPL. It is shown that the accuracy of the integration decreases rapidly during the second heliocentric phase, due essentially to the poor accuracy right after the flyby. The values of the errors are small enough to detect the presence of a second close encounter, but too large to allow us to predict the possibility of an Earth's impact. For this purpose it would be mandatory to refine the dynamical model and to understand why the first close approach provokes such a steep increase in the errors. Nevertheless, regardless of the dynamical model used here, the developed methods are promising and deserve to be described.

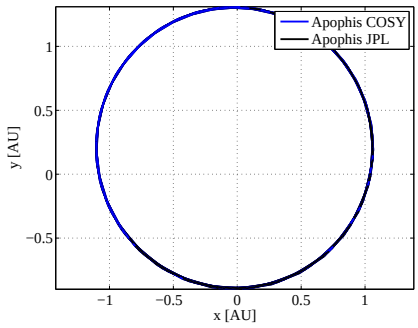

Figure 4.33: Apophis nominal heliocentric trajectory from April 2029 to April 2036.

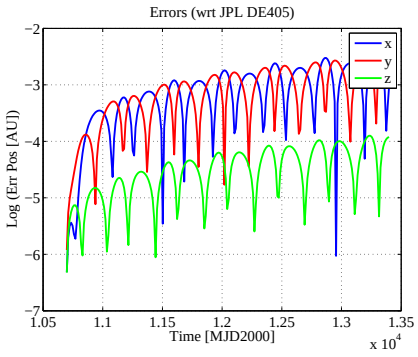

Figure 4.34: Profile of errors on position for Apophis nominal heliocentric phase from April 2029 to April 2036.

The major difficulty of addressing the analysis of the second encounter is

the convergence region of the DA expansion. As Figure 4.35 clearly shows, the evaluation of the Taylor expansion of the flow at the epoch of resonant return delivers a set of positions that span almost the entire Solar System up to Jupiter orbit. This result is only due to Taylor map inaccuracy, as the actual set of possible final positions is more limited, as it will be shown in Section 4.5.1. Furthermore, it has been noticed that increasing the expansion order does not improve the result, confirming that the nonlinearity introduced by the first close encounter cannot be handled by a single Taylor expansion.

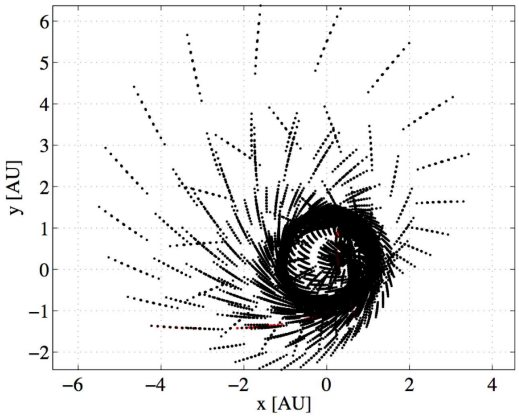

Figure 4.35: Evaluation of the Taylor expansion of the flow at the date of second encounter.

4.5.1 Monte Carlo Analysis

In order to integrate the second heliocentric phase, the solution set after the first flyby is analyzed in details. As clearly shown by Figure 4.36 and 4.37, both the position and velocity sets are stretched along a common axis. Based on this observation, we decided to perform a reference change in order to align the x axis with the stretching direction and to build up new DA variables in these new coordinates. The reference frame is changed by computing the eigenvalues and eigenvectors of the state transition matrix (first order expansion of the flow) and applying the rotation that aligns the eigenvector associated with the maximum eigenvalue with the x axis. By applying this procedure we obtain that the set of Apophis positions and velocities is mainly aligned with the x axis as displayed by Figure 4.38 and 4.39. In particular, the two pictures show the displacements from the nominal solution in the rotated coordinates.

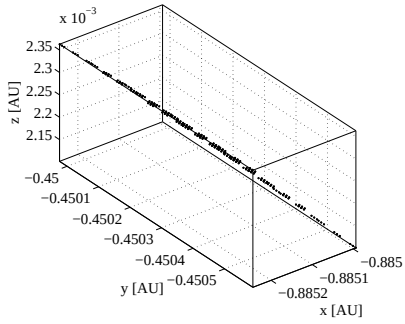

Figure 4.36: Apophis position solution set after the first flyby.

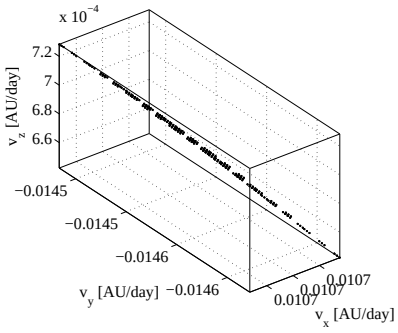

Figure 4.37: Apophis velocity solution set after the first flyby.

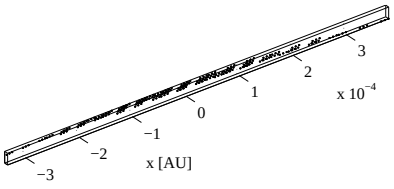

Figure 4.38: Apophis position solution set after the first flyby in the rotated reference frame.

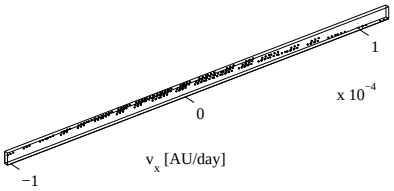

Figure 4.39: Apophis velocity solution set after the first flyby in the rotated reference frame.

The new DA variables are built by simply initializing the initial conditions in order to include the position and velocity sets. These variables are then rotated back to the heliocentric reference frame and propagated for the desired time span. Furthermore, to facilitate the convergence of the Taylor expansions, the component v_x of the velocity is uniformly divided in 10 pieces. Moreover, the flow expansion is also performed with respect to final time as explained in Section 4.3.1, in order to deal with resonant returns that do not exactly happen after seven Earth's revolutions ($t = 13252.67623$ MJD2000).

Figure 4.40 shows the nominal solutions of the ten DA starting conditions, where Figure 4.41 shows the evaluation of the ten flows expansion at the boundaries of the uncertainty boxes. Both these evaluations are performed at the nominal resonant return epoch, as it can be understood by noticing

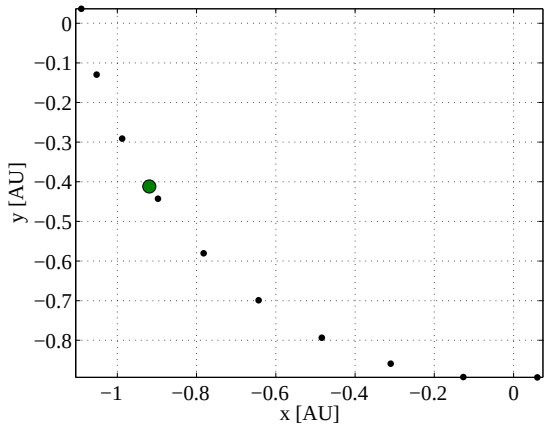

Figure 4.40: Nominal final points at epoch $t = 1.32466 \times 10^4$ MJD2000 (Earth represented by the green circle).

that the green circle representing the Earth's location is fixed.

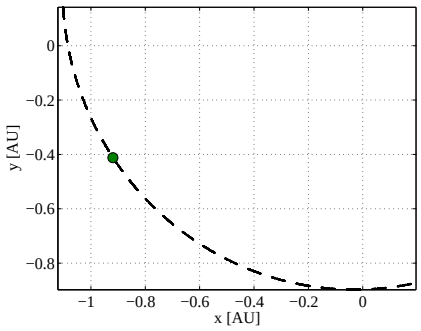

Figure 4.41: Final set of solution at epoch $t = 1.32466 \times 10^4$ MJD2000 (Earth represented by the green circle).

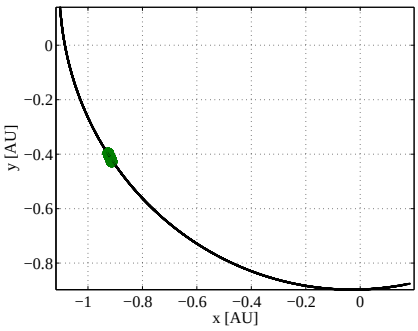

Figure 4.42: Final set solution of 1000 virtual asteroids with uniform distribution at epoch $t = 13252.67623 \pm 1$ MJD2000.

Figure 4.42 is obtained by evaluating the ten flow expansions of 10000 virtual asteroids uniformly distributed on the entire set of rotated initial conditions and considering the final epochs in the range $t = 13252.67623 \pm 1$ MJD2000. It can be seen that Apophis trajectory and Earth trajectory actually intersect in the space dimensions. In order to have a real close encounter this intersection should happen also in time coordinates, and for this reason we report the Apophis-Earth distance in Figure 4.43. Note that only the lower distances, expressed in Earth radii, are displayed. It can be noticed

that the probability of having a close encounter (the Earth's sphere of influence is roughly 160 radii) is quite small (less than 0.8%). Moreover, as the values of minimum CED are of order of 1×10^{-3} AU, which is comparable to the integration accuracy, the current model can only be used to compute the probability of a close encounter. Nothing can be said about the probability of having impacts and about the flyby trajectory. On the other hand, this model is still more accurate than other models that are used for resonant return computation based mainly on Kepler's motion or linear expansions of the flow [27].

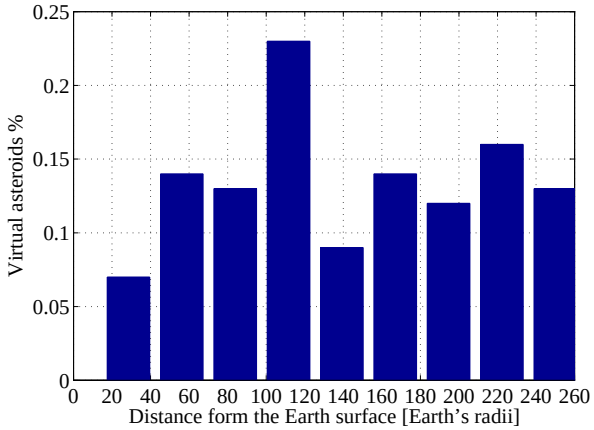

Figure 4.43: Result of Monte Carlo simulation in terms of percetange.

4.5.2 Minimization of Resonant Return Distance

In this section the attention is focused on the subset of initial conditions whose central point is the closest to the 6:7 resonance, as easily identifiable in Figure 4.40. As an output of the post encounter integrations the n-th order Taylor expansion of Apophis' distance from the Earth's center of mass is obtained with the respect of both final time and space variables (by applying the algorithm of Section 4.3.1). This map is used to find the resonant return CED by running the SQP algorithm already used in Section 4.3.3.

The optimization problem has 7 variables (the displacement in both space and time coordinates from the nominal final conditions), 7 upper and lower bounds on their values (to force the initial solution to be compatible with the set of initial conditions). The objective is the Apophis' distance form Earth's center of mass expressed as a 3-rd order Taylor polynomial. The algorithm runs in 0.2 s and computes a minimum resonant return distance of

37465.2 km. The associated initial condition (three days after the first close encounter in 2029) is given in Table 4.5 and showed in Figures 4.44 – 4.47 in both J2000.0 and rotated coordinates reference frames by the red circles.

Table 4.5: Apophis optimized post encounter condition for resonant return.

x^*	-0.885163512703941	AU
y^*	-0.450283961392269	AU
z^*	0.002238751682875	AU
v_x^*	0.010715164746250	AU/day
v_y^*	-0.014612601411040	AU/day
v_z^*	0.000673211849022	AU/day

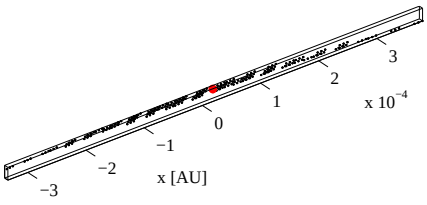

Figure 4.44: Apophis position solution set after the first flyby.

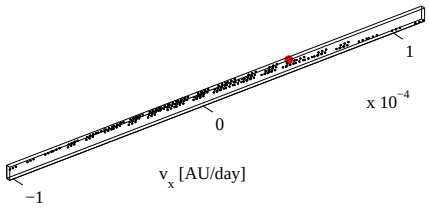

Figure 4.45: Apophis velocity solution set after the first flyby.

Note that the closest encounter occurs 0.5001 days before the exact 7 years resonance condition. It has to be stressed that the computation of the minimum resonant return distance cannot be trusted, unless the integration accuracy is increased. This necessarily requires an increase in the fidelity of the dynamical model implemented for the asteroid's motion description.

4.5.3 Orbital Periods Analysis

An alternative approach for the analysis of resonant returns is addressed in this section, which is mainly based on the imposition of the resonance conditions after the first Apophis Earth's flyby. We start by analyzing the asteroid's orbital parameters at the end of the 2029 Earth's flyby, defined by the initial values of the orbital parameters $(a_i, e_i, i_i, \Omega_i, \omega_i, E_i)$. The DA-based

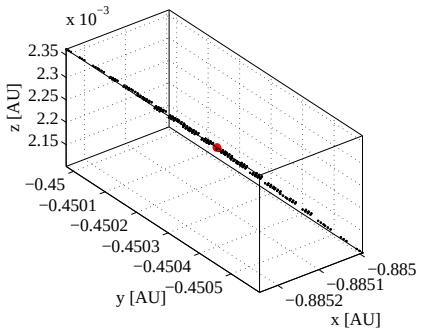

Figure 4.46: Apophis position solution set after the first flyby in the rotated reference frame.

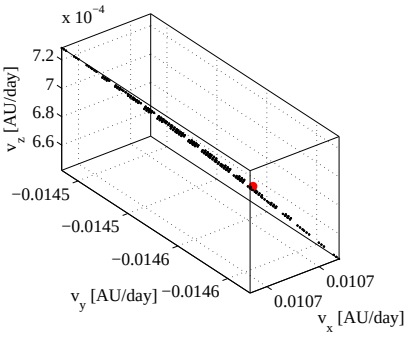

Figure 4.47: Apophis velocity solution set after the first flyby in the rotated reference frame.

RKF78 integrator is then run to obtain the Taylor expansion of the flow at the exits of Earth's sphere of influence; i.e., three days after the epoch of the nominal close encounter. The flow is used to compute the Taylor expansion of the exit orbital parameters $(a^+, e^+, i^+, \Omega^+, \omega^+, E^+)$ with respect to their initial values:

$$\begin{pmatrix} a^+ \\ e^+ \\ i^+ \\ \Omega^+ \\ \omega^+ \\ E^+ \end{pmatrix} = \begin{pmatrix} \mathcal{M}_{a^+} \\ \mathcal{M}_{e^+} \\ \mathcal{M}_{i^+} \\ \mathcal{M}_{\Omega^+} \\ \mathcal{M}_{\omega^+} \\ \mathcal{M}_{E^+} \end{pmatrix} \begin{pmatrix} \delta a_i \\ \delta e_i \\ \delta i_i \\ \delta \Omega_i \\ \delta \omega_i \\ \delta E_i \end{pmatrix} . \tag{4.35}$$

Given the set of uncertain initial conditions defined in Table 4.1, the LDB algorithm introduced in Section 4.3.3 is used to get validated lower and upper bounds for the range of the exit orbital parameters, which are reported in Table 4.6. The widths of the resulting interval enclosures are shown in Table 4.7. As it can be seen, the resulting widths are between two and six orders of magnitude greater than the $3\,\sigma$ values used to set up the initial conditions in 2020 (see Table 4.1 for comparison). As already highlighted in the previous section, they are too wide to be propagated through long-term integrations. This precludes the possibility of integrating the whole set at once to check for the occurrence of resonant returns. The previous section dealt with this problem by cutting the initial set in pieces and propagate them separately. In this section we try to shrink the set to be integrated by imposing suitable constraints. This approach is based on the idea that, after the first flyby, we are only interested in the propagation of those conditions that could lead to a resonant return.

Table 4.6: Interval enclosures of the possible values of the orbital parameters after Earth's flyby.

Parameter	Validated enclosure	
a^+	$[1.0885248608329950, 1.1167855278894610]$	AU
e^+	$[0.1850331124357293, 0.1936692486068235]$	–
i^+	$[0.0361778486454323, 0.0414888046454464]$	rad
Ω^+	$[3.5540081276430700, 3.5544917568577770]$	rad
ω^+	$[1.1903178905464240, 1.3061022370129520]$	rad
E^+	$[5.2060286718957850, 5.3209185579389790]$	rad

Table 4.7: Widths of the interval enclosures of Table 4.6.

Parameter	Width	
a^+	$2.826066705646602 \cdot 10^{-2}$	AU
e^+	$8.636136171094183 \cdot 10^{-3}$	–
i^+	$5.310956000014064 \cdot 10^{-3}$	rad
Ω^+	$4.836292147061272 \cdot 10^{-4}$	rad
ω^+	$1.157843464665271 \cdot 10^{-1}$	rad
E^+	$1.148898860431939 \cdot 10^{-1}$	rad

The scientific community has devoted major effort to study the Apophis' resonant return to Earth in 2036, which corresponds to a resonance 6:7 between Apophis' and Earth's orbits. In the framework of the two-body problem, this resonant return condition translates into the constraint

$$a^+ = \left(\frac{7}{6}\right)^{\frac{2}{3}} a_E = 1.108233415430825 \text{ AU} = \overline{a}, \tag{4.36}$$

where a^+ is Apophis' semi-major axis after Earth's flyby and a_E is Earth's semi-major axis. It is worth observing that $\overline{a}$ belongs to the interval enclosure for the possible Apophis' exit semi-major axis. This means that there are possibilities for a 6:7 resonant return in 2036. Although the condition (4.36) is strictly valid on a two-body dynamical framework, we start imposing it on the exit conditions to check the resulting Apophis' position after seven years.

To this aim, similarly to the approach followed for the identification of the ILC in Section 4.4, the constraint 4.36 is used to identify the associated constraint manifold in the space of the initial conditions. More specifically,

the first component of the map (4.35) is used to build the following map:

$$\begin{pmatrix} a^+ \\ \delta e_i \\ \delta i_i \\ \delta\Omega_i \\ \delta\omega_i \\ \delta E_i \end{pmatrix} = \begin{pmatrix} \mathcal{M}_{a^+} \\ \mathcal{I}_{e_i} \\ \mathcal{I}_{i_i} \\ \mathcal{I}_{\Omega_i} \\ \mathcal{I}_{\omega_i} \\ \mathcal{I}_{E_i} \end{pmatrix} \begin{pmatrix} \delta a_i \\ \delta e_i \\ \delta i_i \\ \delta\Omega_i \\ \delta\omega_i \\ \delta E_i \end{pmatrix}, \tag{4.37}$$

where $\mathcal{I}_{e_i}$, $\mathcal{I}_{i_i}$, $\mathcal{I}_{\Omega_i}$, $\mathcal{I}_{\omega_i}$, $\mathcal{I}_{E_i}$ are the identity maps for e_i, i_i, Ω_i, ω_i, E_i, respectively. The map (4.37) is then inverted to obtain

$$\begin{pmatrix} \delta a_i \\ \delta e_i \\ \delta i_i \\ \delta\Omega_i \\ \delta\omega_i \\ \delta E_i \end{pmatrix} = \begin{pmatrix} \mathcal{M}_{a^+} \\ \mathcal{I}_{e_i} \\ \mathcal{I}_{i_i} \\ \mathcal{I}_{\Omega_i} \\ \mathcal{I}_{\omega_i} \\ \mathcal{I}_{E_i} \end{pmatrix}^{-1} \begin{pmatrix} a^+ \\ \delta e_i \\ \delta i_i \\ \delta\Omega_i \\ \delta\omega_i \\ \delta E_i \end{pmatrix}. \tag{4.38}$$

The constraint (4.36) can then be imposed as

$$\begin{pmatrix} \delta a_i \\ \delta e_i \\ \delta i_i \\ \delta\Omega_i \\ \delta\omega_i \\ \delta E_i \end{pmatrix} = \begin{pmatrix} \mathcal{M}_{a^+} \\ \mathcal{I}_{e_i} \\ \mathcal{I}_{i_i} \\ \mathcal{I}_{\Omega_i} \\ \mathcal{I}_{\omega_i} \\ \mathcal{I}_{E_i} \end{pmatrix}^{-1} \begin{pmatrix} \overline{a} \\ \delta e_i \\ \delta i_i \\ \delta\Omega_i \\ \delta\omega_i \\ \delta E_i \end{pmatrix}. \tag{4.39}$$

The first component of the map (4.39), which will be indicated as

$$\delta a_i = \mathcal{M}_{a_i}(\delta e_i, \delta i_i, \delta\Omega_i, \delta\omega_i, \delta E_i), \tag{4.40}$$

is the arbitrary order Taylor expansion of the constraint manifold associated to the condition (4.36); i.e., given any e_i, i_i, Ω_i, ω_i, E_i in the set of the possible initial conditions, the evaluation of the map (4.40) delivers the correction δa_i for $\tilde{a}_i = a_i^0 + \delta a_i$. This is the initial semi-major axis Apophis must have in 2020 to have a resonant return to Earth in 2036.

The map (4.40) can be inserted in map (4.35) to obtain

$$\begin{pmatrix} a^+ \\ e^+ \\ i^+ \\ \Omega^+ \\ \omega^+ \\ E^+ \end{pmatrix} = \begin{pmatrix} \tilde{\mathcal{M}}_{a^+} \\ \tilde{\mathcal{M}}_{e^+} \\ \tilde{\mathcal{M}}_{i^+} \\ \tilde{\mathcal{M}}_{\Omega^+} \\ \tilde{\mathcal{M}}_{\omega^+} \\ \tilde{\mathcal{M}}_{E^+} \end{pmatrix} \begin{pmatrix} \delta e_i \\ \delta i_i \\ \delta\Omega_i \\ \delta\omega_i \\ \delta E_i \end{pmatrix}, \tag{4.41}$$

which is the Taylor expansion of the exit conditions when the 6:7 resonance is imposed. However, a better analysis of the map (4.40) shows that some pruning on the set of initial conditions must be performed. The LDB algorithm is used again to obtain validated lower and upper bounds for the initial semi-major axis resulting from the equation (4.40). More specifically, the map $\tilde{a}_i = \mathcal{M}_{\tilde{a}_i}(\delta e_i, \delta i_i, \delta\Omega_i, \delta\omega_i, \delta E_i)$ is computed using equation (4.40). Then, given the $3\,\sigma$ values for e_i, i_i, Ω_i, ω_i, and E_i reported in Table 4.1, the LDB algorithm is used to obtain the interval enclosure

$$\tilde{a}_i \in [\,0.936366604293064,\, 0.9363670385434669\,]\ \text{AU}. \tag{4.42}$$

For the sake of a easier comparison, the set of possible values for a_i defined in Table 4.1 is reported here in interval format:

$$a_i \in [\,0.936366882199485,\, 0.936367019899485\,]\ \text{AU}. \tag{4.43}$$

As it can be seen from (4.42) and (4.43), the interval for $\tilde{a}_i$ includes the interval for a_i. This confirm that 6:7 resonance conditions are included in the set of Apophis' initial conditions reported in Table 4.1. On the other hand, this result highlights an overestimation problem (the interval on $\tilde{a}_i$ is 3.15 times wider than the original interval on a_i). By inserting the map (4.40) in map (4.35), we take the effects of $\tilde{a}_i$ into account when evaluating the exit conditions. Consequently, if we consider the whole set of possible initial conditions for e_i, i_i, Ω_i, ω_i, and E_i, we will have resonant exit conditions that include the effects of the whole interval in equation (4.42). This evidently overestimates the actual set of initial semi-major axis values to be propagated.

In order to mitigate this overestimation problem, the following observation is utlized. The reason of the previous overestimation is that the value of $\tilde{a}_i$ corresponding to some parts of the five-dimensional set of initial conditions for e_i, i_i, Ω_i, ω_i, E_i is outside of the set of admissible values for the initial semi-major axis reported in equation (4.43). Consequently, the overestimation could be mitigated by pruning away these parts of the five-dimensional set. Based on this observation, the following pruning procedure is implemented. The intervals for e_i, i_i are first split into N subintervals, whereas the intervals on Ω_i, ω_i, and E_i are left unchanged. This allow the five-dimensional set to be split into $N \times N$ boxes. For each box, the resulting values for $\tilde{a}_i$ are computed by evaluating the map (4.40), and upper and lower bounds are obtained using the LDB algorithm. If the intersection between the enclosure and the interval (4.43) is empty, the box is pruned. Otherwise, the interval of the third variable Ω_i is split into N subintervals, and the resulting smaller boxes are processed. The process continues until

Table 4.8: Interval enclosures of the possible values of the orbital parameters after Earth's flyby when the 7:6 resonance is imposed.

Parameter	Validated enclosure	
e^+	$[0.190877337891586, 0.190909812844946]$	–
i^+	$[0.037781098441056, 0.037965023439218]$	rad
Ω^+	$[3.554158924526159, 3.554189121821580]$	rad
ω^+	$[1.223742330063934, 1.223911990903699]$	rad
E^+	$[5.287657593878502, 5.287765068425091]$	rad

the intervals on all five orbital parameters are split. The final result is a list of admissible boxes that are used to compute Apophis' exit conditions using map (4.41). The interval obtained from a pruning process with $N = 20$ is

$$(\tilde{a}_i)_{N=20} \in [\,0.936366807028420,\, 0.936367038543463\,] \text{ AU}. \tag{4.44}$$

By throwing away about half of the five-dimensional set of initial conditions (1221520 of 3200000 boxes remain after pruning), the pruning process significantly reduces the overestimation problem, as the interval on $(\tilde{a}_i)_{N=20}$ is 1.68 times wider than the interval on a_i. This interval is used in the followings. Even if it still overestimates the set of a_i, the overestimation is acceptable, especially considering that it can be deemed as a conservative hypothesis: if the occurrence of an impact in 2036 can be discarded using the set of $\tilde{a}_i$, then it cannot occur even with the actual set of a_i.

The map (4.41) is then used to obtain interval enclosures of Apophis' exit conditions when the resonance is imposed. More specifically, the LDB algorithm is used to estimate the range of e^+, i^+, Ω^+, ω^+, and E^+ over each box remaining after the pruning process. Then, the resulting ranges are enveloped. The final result is reported in Table 4.8. The intervals of Table 4.8, together with the resonance conditions (4.36) for a^+ are used to set up new DA variables for the exit orbital parameters $(a^+, e^+, i^+, \Omega^+, \omega^+, E^+)$ that will be used as initial conditions for a DA-based integration of Apophis' dynamics from 2029 to 2036. It is worth observing that the size of the new box to be propagated is significantly smaller than the one highlighted in Table 4.8, and the interval widths (see Table 4.9) are only from one to two orders of magnitude greater than the intervals for $(a_i, e_i, i_i, \Omega_i, \omega_i, E_i)$ in 2020. A 6-th order DA-based integration allows a precise uncertainty propagation to be achieved.

The propagation of the new uncertainty set is now analyzed. The result of the integration is the Taylor expansion of Apophis' position and velocity

Table 4.9: Widths of the interval enclosures of Table 4.8.

Parameter	Width	
e^+	$1.623747667969800 \cdot 10^{-5}$	–
i^+	$9.196249908074300 \cdot 10^{-5}$	rad
Ω^+	$1.509864771054300 \cdot 10^{-5}$	rad
ω^+	$8.483041988283090 \cdot 10^{-5}$	rad
E^+	$5.373727329421870 \cdot 10^{-5}$	rad

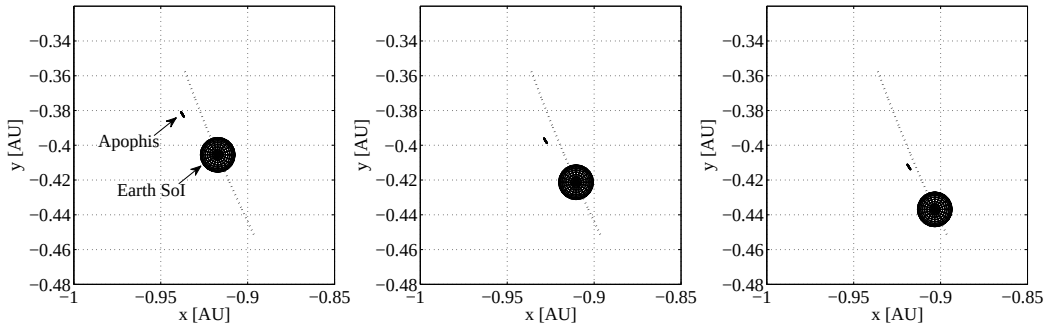

Figure 4.48: Apophis 2036 close encounter: resonance imposed after 7 years.

at the final epoch with respect to $(e^+, i^+, \Omega^+, \omega^+, E^+)$. Three final epochs are considered for the sake of a better analysis:

$$\begin{aligned} t_f^0 &= t_{res} \\ t_f^1 &= t_{res} + 1 \text{ day} \\ t_f^2 &= t_{res} + 2 \text{ day} \\ t_f^3 &= t_{res} + 3 \text{ day}, \end{aligned} \tag{4.45}$$

where t_res is the epoch of the exact resonance in 2036. For each final epoch in equation (4.45), the map is evaluated at 10000 random virtual asteroids selected with uniform distribution. The result is plotted in Figure 4.48.

As can be noticed from Figure 4.48, no virtual asteroid enters Earth's sphere of influence, so indicating that there is no hazardous close encounter in 2036. However, keeping in mind that much effort must be spent in future work to improve the accuracy of the dynamical model, two major limitations preclude our analysis from claiming general results. A first limitation is the integration error, which has been shown not to be acceptable after the first Earth's flyby. This problem will be carefully addressed in future

developments. The second major limitation is based on the observation that the resonance conditions have been imposed by relying on a two-body problem. However, Apophis' motion is described in an n-body dynamics during integrations, including further perturbations. Consequently, a correction to the resonance condition (4.36) must be implemented to take into account of the actual dynamics. To this aim, we correct the exact resonance condition (4.36) by allowing the resonance to occur at an epoch different but close to the exact resonance epoch t_f^0. The exact resonance condition (4.36) is corrected into

$$a^+ = \left(\frac{7}{6} a_E^{\frac{2}{3}} + \frac{\delta t_f}{6} \frac{\sqrt{\mu_{Sun}}}{2\pi} \right)^{\frac{2}{3}}, \tag{4.46}$$

where δt_f takes into account for resonance at epochs $t_f \neq t_f^0$. The variable δt_f is initialized as a new DA variable. Consequently, it appears in all the maps from (4.39) to (4.41), so increasing the size of the boxes for $(a^+, e^+, i^+, \Omega^+, \omega^+, E^+)$. The results of the new integrations from 2029 to 2036 are shown in Figures 4.49 - 4.51, where δt_f is fixed to +1, +2, and +3 day, respectively. In this case some of the virtual asteroids enter Earth's sphere of influence. However, the nonlinearities associated to the propagation of the hyperbolic passage do not show up. This is deemed to be associated to the inaccuracy of the DA representations of Apophis' position for regions far from the reference point for the expansions. Further analyses are needed to study this accuracy problem. Nevertheless, similarly to the previous section, the resulting maps can be used to minimize Apophis' distance from Earth in 2036 in order to identify possible close encounters.

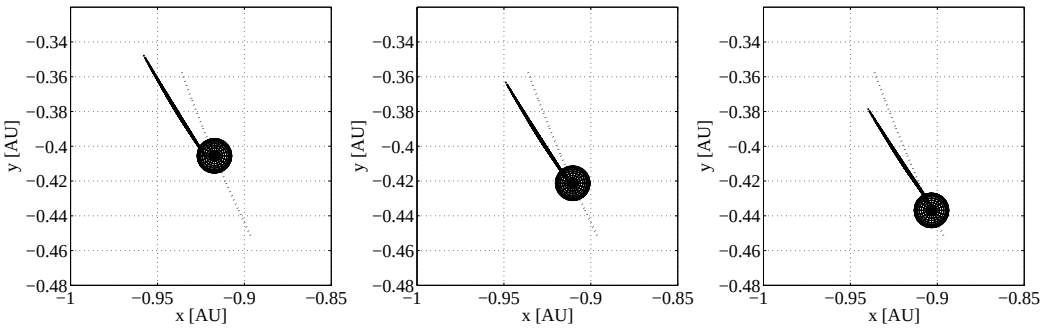

Figure 4.49: Apophis 2036 close encounter: resonance imposed after 7 years ± 1 day.

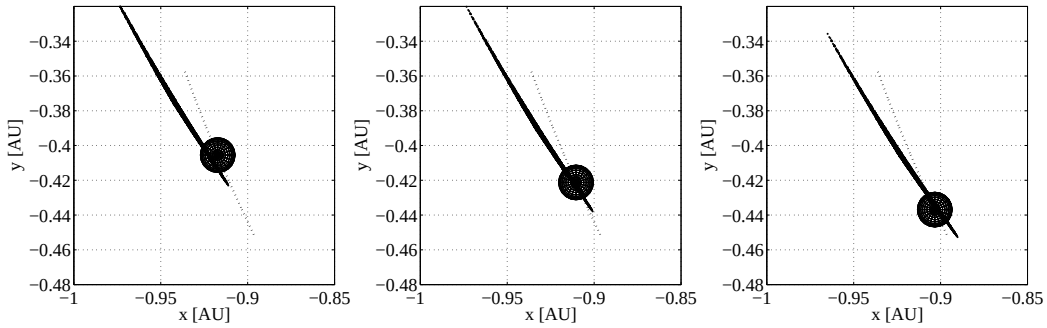

Figure 4.50: Apophis 2036 close encounter: resonance imposed after 7 years ± 2 days.

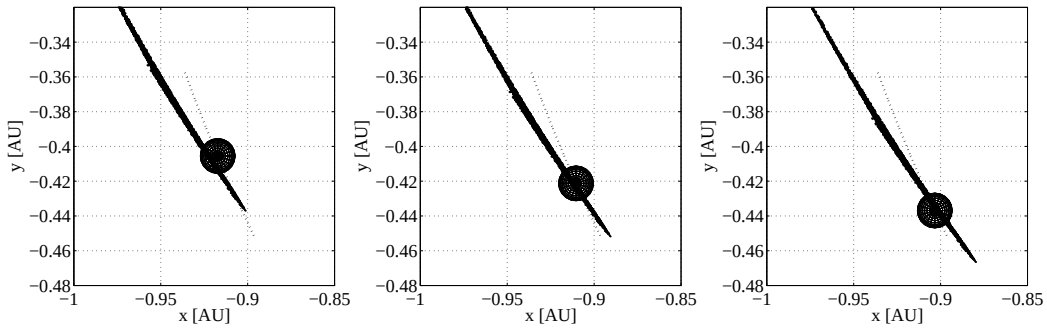

Figure 4.51: Apophis 2036 close encounter: resonance imposed after 7 years ± 3 days.

Chapter 5

Validated Integration of Solar System Dynamics

This chapter describes the results obtained for the validated integration of Solar System dynamics with both the old and the new validated integration tools.

5.1 Old Taylor Model Integrator

The results obtained with the old version of the validated integrator described in Section 2.4.1 are presented. The integration is performed using the same initial conditions as the DA integrations. In particular, the uncertainty set defined on cartesian coordinates is considered. The initial Taylor models are obtained from the initial DA variables used in the previous chapter by adding arbitrarily small remainder bounds. In order to optimize the computational cost of the integration a 20-th order expansion in time and 6-th order in space are selected. A high order expansion in time is required to manage integration step-sizes compatible with the integration of Solar System dynamics, whereas a 6-th order in space is needed to avoid rapid groth of the remainder bound. Furthermore, the QR preconditioning and shrink wrapping algorithms are used to handle the long-term integration.

As already done for DA integration, the heliocentric phase is integrated in the Solar System barycentric reference frame, whereas the close encounter in the geocentric reference frame. The three different models of the ephemerides are used, starting from the simple model based on osculating ellipses up to the one based on the highly accurate cubic spline.

The first results are those obtained with the osculating ellipses ephemeris function. Figure 5.1 shows the accuracy of the nominal solution during the

heliocentric phase, by comparing it with JPL Horizons system. The errors at the end of this phase are of the order 10^{-2} AU, large enough to totally mispredict the close encounter. In Figure 5.2 it is apparent that the asteroid never enters the Earth's sphere of influence, as the trajectory is unaffected by the Earth gravitational field. It is worth noting that, although the adopted model is not appropriate for studying the close encounter, it is shown that Taylor models enable the validated integration of complex dynamical systems for large time intervals (several orbital revolutions). This is a major result considering that all the interval methods would fail due to the dependency problem and wrapping effects as shown in [24].

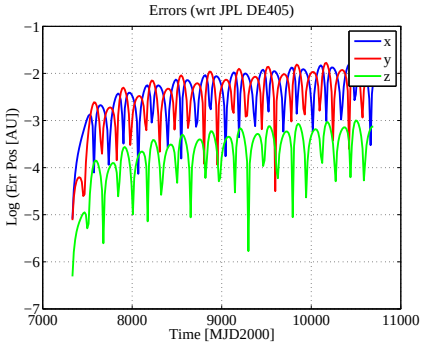

Figure 5.1: Accuracy of the validated integration of heliocentric phase using ellipses ephemerides.

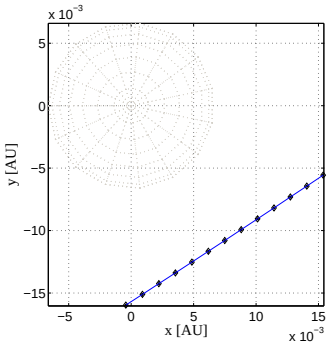

Figure 5.2: Validated integration of the close encounter using ellipses ephemerides..

During the integration, the selected step-size is always the maximum allowed of 10 days, a choice that is necessary to avoid algebraic failures in the evaluation of the ephemeris function. Note that in all the pictures, the results are given as interval enclosure of the computed Taylor models, thus an overestimation of the actual volume is presented.

The second integration is performed using the Fourier ephemeris model. Figure 5.3 shows integration errors of one order lower than those obtained with the osculating ellipses ephemerides. As a result, the validated trajectory of Apophis enters the Earth's sphere of influence, and a close encounter occurs. On the other hand, the details of the flyby are not captured by this dynamical model, as it can be observed by comparing Figure 5.4 with Figure 4.5. The integration of the close encounter fails when the asteroid is approximately at the flyby pericenter. The reasons of this failure can be assumed to lie in

- an increase in the nonlinearity of the dynamics,

- cancellation errors in the evaluation of planetary ephemerides due to time offsets and in the computation of bodies relative distance due to subtraction of comparable values,

- operations that provoke an artificial inflation of the remainder bound (e.g sequence of division and multiplication for large numbers).

These problems have been properly addressed when the new validated integrator is applied to the flyby integration, as detailed in the next section.

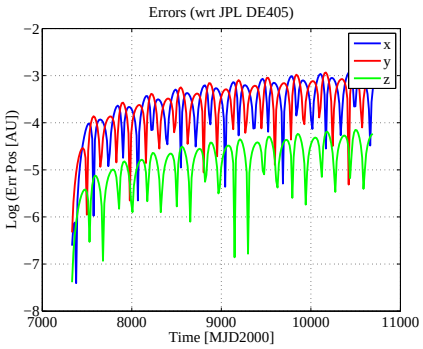

Figure 5.3: Accuracy of the validated integration of heliocentric phase using Fourier ephemerides.

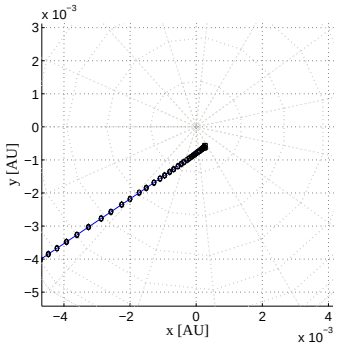

Figure 5.4: Validated integration of the close encounter using Fourier ephemerides.

Figure 5.5 gives a detail of the interval enclosure of the Taylor model just before the failure of the integration.

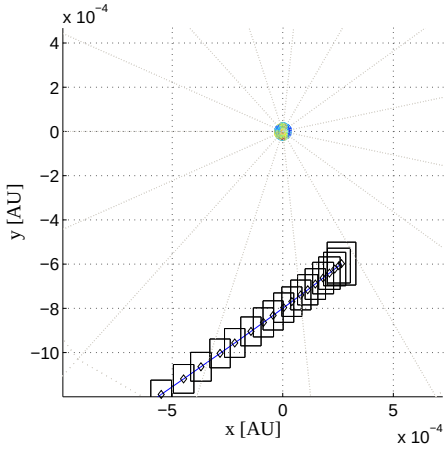

Figure 5.5: Details of the validated integration of the close encounter using Fourier ephemerides.

The last test case is the validated integration using cubic spline ephemerides. Both the heliocentric and the geocentric phases of Figure 5.6 and 5.7 are comparable with those obtained with DA-based RKF78 integration. Also in this case an algebraic failure occurs approximately at the pericenter of the flyby.

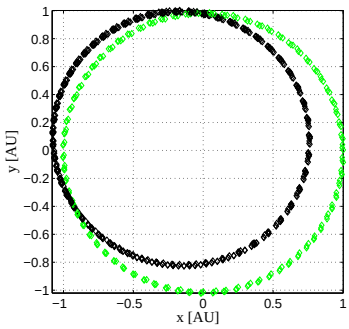

Figure 5.6: Apophis validated heliocentric trajectory (black) and Earth trajectory (green).

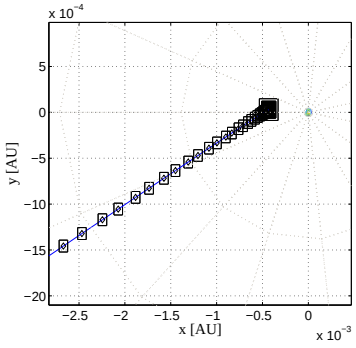

Figure 5.7: Details of Apophis validated integration of close encounter.

Figure 5.8 and 5.9 show the interval enclosures of the initial and final interval models of the asteroid flyby. Note that after the 9 years integration prior to the close encounter there is no significant inflation of the Taylor model size. On the other hand, the artificial inflation of the Taylor model is apparent just before the integration failure for the same reasons explained previously.

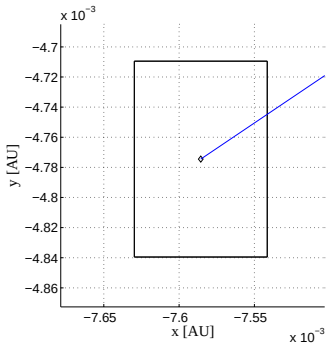

Figure 5.8: Apophis close encounter starting box.

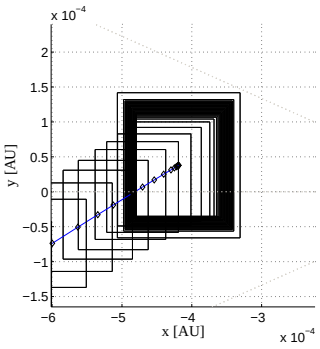

Figure 5.9: Apophis close encounter final box before failure.

5.2 New Taylor Model Integrator

In Section 5.1 it has been shown that the validated integrator can easily compute the heliocentric phase of the trajectory, whereas it fails to compute the flyby. For this reason this section presents some preliminary results obtained by applying the new validated integrator to the flyby phase only. The initial conditions here are taken from the DA-based integration three days prior to the closest approach. These DA conditions are then artificially converted into Taylor models by adding arbitrary small remainder bounds.

The integration is performed in the geocentric reference frame, considering only the asteroid, the Earth, and the Sun as gravitational bodies, i.e. a restricted three body problem is integrated. This simplification is necessary in understanding how the dynamical model must be coded to avoid a numerical inflation of the remainder bound.

The main numerical tricks necessary to address this integration were

- shifting time coordinate in such a way that $t = 0$ at the closest encounter;
- computing the ephemerides in the units used for the description of the dynamical model ($R_E = 1$ and $\mu_E = 1$), thus avoiding scaling in ODE right hand side evaluation;
- using ad hoc functions for the computation of the inverse of the square root of the radius;
- avoiding cancellation errors by writing the initial conditions of Apophis in the geocentric coordinate, thus the repetitive subtraction of Apophis and Earth coordinates is not necessary;
- avoiding all other numerics that produce a loss of accuracy; e.g., the repetition of TM operations and the sequence of division and multiplications a TM for large numbers.

Figure 5.10 and 5.11 show the result of the validated integration of the Apophis flyby using the new validated integration and considering uncertainties on initial orbital parameters. The integration is performed using 29-th order expansion in time and 9-th in transversal coordinates. It is apparent that the integrator can manage the high nonlinearities that characterize the flyby dynamics. Note that the interval enclosure of the TM representation of the flow is used for visualization aims (the black boxes). The actual volume of the TM is much smaller as indicated by the blue dots, which are the evaluation of the TM representation of the flow for a set of initial uncertainties.

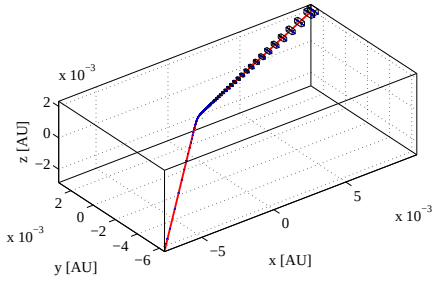

Figure 5.10: Apophis flyby validated integration: nominal solution (red line), interval enclosure of the TM (black box), and TM evaluations (blue dots).

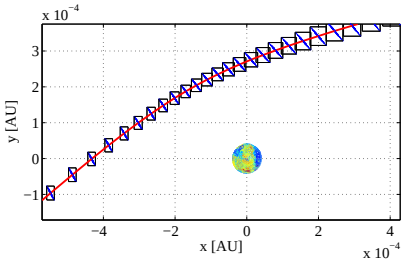

Figure 5.11: Details of Apophis flyby validated integration.

Figure 5.12 shows that the maximum remainder error size at the end of the integration is around 10^{-10}, meaning that the flow dependency on the initial conditions is almost totally described by the polynomial part of the TM. In order to keep the remainder bound error size small during the integration, the step size must reduce when the high nonlinearities of the dynamics show up. This effect is clearly shown in Figure 5.13. In particular, the step size reaches the minimum value of 8×10^{-3} at the closest encounter epoch. The computational time of the integration is 6544 s on a Intel Pentium Dual Core 2.0 GHz, RAM 1 GHz, MacBook laptop.

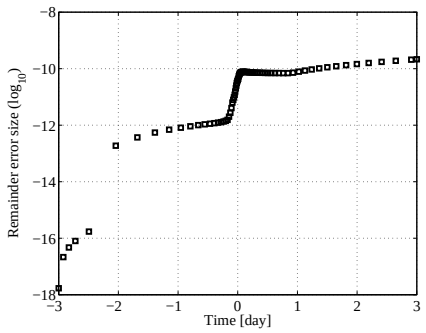

Figure 5.12: Maximum remainder error size for Apophis flyby validated integration.

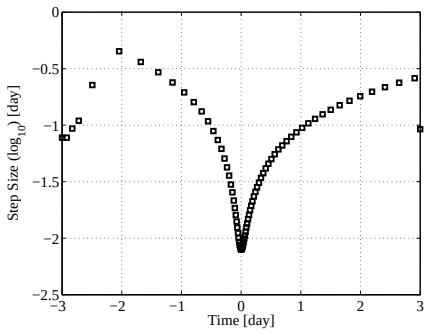

Figure 5.13: Step size profile for Apophis flyby validated integration.

Figure 5.14 and 5.15 show the result of the validated integration of Apophis

flyby considering uncertainties on initial cartesian coordinates. It is clear that, being that the set of initial conditions is bigger, the problem of obtaining a validated propagation is more challenging. It can be noticed that a box split occurs right before the close encounter in order to reduce the nonlinear terms necessary to describe the flow. In this way, the maximum size

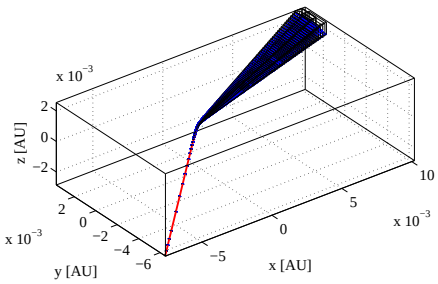

Figure 5.14: Apophis flyby validated integration: nominal solution (red line), interval enclosure of the TM (black box), and TM evaluations (blue dots)

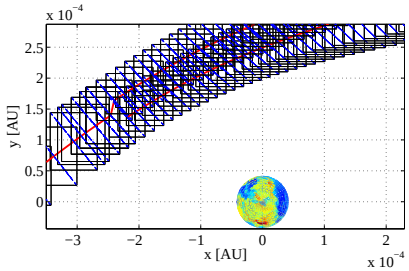

Figure 5.15: Details of Apophis flyby validated integration.

of the remainder error is kept suitably small, as shown by Figure 5.16. The computational time rises to 32136 s on the same machine used before. This high value is essentially due to the small stepsizes required after the close encounter (see Figure 5.17) and to the propagation of two TM objects after the domain splitting occurs. Note that the computational time could have been considerably lowered by running the integration on parallel machines.

When the asteroid trajectory propagation is addressed by means of a rigorous integrator there is no need to develop algorithms for the identification of impact occurrence. This result is immediately obtained by looking for intersections between the validated enclosure of the trajectory of the NEO and the Earth. From Figures 5.11 and 5.15 it is clear that, for the considered set on initial conditions and within the implemented dynamical model, the probability of Apophis impact with the Earth in 2029 is zero. Furthermore, within the model used, the achieved result is rigorous.

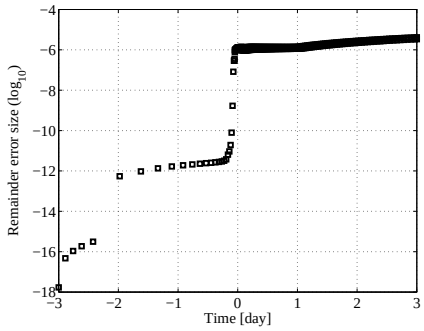

Figure 5.16: Maximum remainder error size for Apophis flyby validated integration.

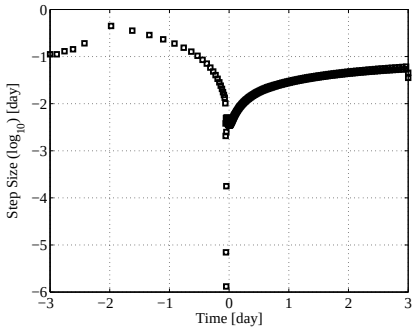

Figure 5.17: Step size profile for Apophis flyby validated integration.

Chapter 6

Conclusions

The work addressed the development of techniques based on differential algebra and Taylor models for the efficient study of NEO close encounters with Earth. Apophis close encounter in 2029 and the resonant return in 2036 were used as test cases. The work performed within the contract can be subdivided in

- the implementation of the dynamical models and ephemeris function,
- the development of a set of tools for close encounters analysis using DA,
- the validated propagation of the asteroid motion using both the old and the new TM-based integrator.

The dynamics of the asteroid have been described in the restricted $(n+1)$-body approximation, in which n includes the Sun, the planets, and the Moon. Furthermore, the relativistic effects and diurnal Yarkovski have been taken into account. The equations of motion have been written both in an inertial reference frame centered in Solar System barycenter and in a non-inertial geocentric reference frame in order to manage the close encounter more easily. In the latter case, relativistic effects have been neglected. Three different ephemeris models were carried out in order to be compatible with DA and TM evaluation. These models consist of a simple osculating ellipses approximation and of a Fourier and cubic spline interpolation of JPL DE405 ephemerides.

DA was used to efficiently obtain high order expansions of the flow of the dynamics with respect to initial conditions. Both uncertainties on Apophis initial orbital parameters and initial cartesian coordinates were considered, compatible with NEO typical measurements accuracy. It was shown that

DA is computationally efficient and that the dynamical models developed are sufficiently accurate to analyze the details of the first Apophis close encounter. On the other hand, a more accurate modeling is required to assess the hazard associated to resonant returns. A set of tools were developed, including:

1. a computationally efficient Monte Carlo simulation algorithm based on a single DA integration and thousands flow map evaluations,

2. a technique based on Taylor map inversion for the automatic computation of both Earth's close encounter distances and epochs for all the virtual asteroids belonging to the initial uncertainty cloud,

3. an impact leading condition algorithm that delivers, at any desired epoch, the initial conditions that lead to an Earth's impact,

4. methods for identifying conditions that lead to hazardous resonant returns.

It was shown that DA can be used either to improve the numerical efficiency (e.g, of Monte Carlo simulations) or to surpass the limitations (e.g., linear expansion of the flow) of already existing methods, as well as to develop brand-new algorithms.

TM-based integration schemes were employed to obtain the validated integration of Apophis motion. It was shown that both the old and the new integration schemes outperform the validated schemes based on interval analysis. In particular, TM-based integrators are capable of integrating wide sets of initial conditions for several orbital revolutions without overestimating the result. Only the new tool was able to perform the the validated integration of the close encounter. The new flow operator, step size control, and dynamic domain decomposition enable the management of the high nonlinearities of the dynamics, even when a large set of initial conditions is propagated.

Future work will be aimed at the implementation of other non-gravitational perturbations (e.g., seasonal Yarkovski and solar radiation pressure effects), at the development of a highly accurate TM-based ephemeris model, at better tailoring the implementation of the dynamics to the TM evaluation, and at implementing the current version of the validated integrator with high precision.

Bibliography

[1] Chesley, S.R. and Milani A.: An automatic Earth-asteroid collision monitoring system, Bull. Am. Astron. Soc., Vol. 32, 2000.

[2] Chodas, P.W. and Yeomans, D.K.: Predicting close approaches and estimating impact probabilities for near-Earth pnjects, Paper AAs 99-462, AAs/AIAA Astrodynamics Specialists Conference, Girdwood, Alaska, 1999.

[3] Milani, A., Chesley, S.R., Valsecchi, G.B.: Astreoid close encounters with Earth: Risk assessment. Planet. Space Sci., Vol. 48, pp. 945–954, 2000.

[4] Berz, M.: Modern Map Methods in Particle Beam Physics, Academic Press, San Diego, 1999.

[5] Makino, K.: Rigorous Analysis of Nonlinear Motion in Particle Accelerators, PhD thesis, Michigan State University, East Lansing, Michigan, USA, 1998.

[6] Berz, M.: The new method of TPSA algebra for the description of beam dynamics to high orders, Technical Report AT-6:ATN-86-16, Los Alamos National Laboratory, 1986.

[7] Berz, M.: The method of power series tracking for the mathematical description of beam dynamics, Nuclear Instruments and Methods A258, 431, 1987.

[8] Berz, M.:High-Order Computation and Normal Form Analysis of Repetitive Systems, Physics of Particle Accelerators, Vol. AIP 249, pp. 456, 1991.

[9] Berz, M., and Makino, K.: COSY INFINITY version 9 reference manual, MSU Report MSUHEP-060803, Michigan State University, East Lansing, MI 48824, 2006.

[10] Makino, K., and Berz, M.: Remainder differential algebras and their applications. In Berz, M., Bischof, C., Corliss, G., and Griewank, A., editors, Computational Differentiation: Techniques, Applications, and Tools, pp. 63–74, Philadelphia, 1996. SIAM.

[11] Moore, R.E.: Methods and Applications of Interval Analysis, SIAM, 1979.

[12] Kulisch, U.W., and Miranker, W.F.: Computer Arithmetic in Theory and Practice, Academic Press, New York, 1981.

[13] Alefeld, G. and Herzberger, J.: Introduction to Interval Computations, Academic Press, 1983.

[14] Moore, R.E.: Reliability in computing: the role of interval methods in scientific computing, Academic Press, 1988.

[15] Kearfott, R.B., Rigorous Global Search: Continuous Problems, Kluwer, 1996.

[16] Makino, K., and Berz, M.: Efficient control of the dependency problem based on Taylor model methods, Reliable Computing, pp. 3–12, 1999.

[17] Berz, M., and Makino, K.,. Verified integration of ODEs and flows with differential algebraic methods on Taylor models. *Reliable Computing*, 4:361–369, 1998.

[18] Berz, M., Makino, K.: Suppression of the wrapping effect by Taylor model-based verified integrators: Long-term stabilization by shrink wrapping, International Journal of Differential Equations and Applications, 2006.

[19] Makino, K., Berz, M.: Suppression of the wrapping effect by Taylor model-based verified integrators: Long-term stabilization by preconditioning, International Journal of Differential Equations and Applications, 2006.

[20] Berz M. and Makino K.: Lecture Notes, Course Presented at Department of Mathematics, University of Barcelona, June 2008, MSUHEP-080609, Michigan State University, 2008.

[21] Seidelmann, P.K.: *Explanatory Supplement to the Astronomical Almanac.* University Science Books, Mill Valley, California, 1992.

[22] Vokrouhlicky, D., Milani, A., Chesley, S.R.: Yarkovsky Effect on small Near-Earth Asteroids: Mathematical Formulation and Examples, Icarus 148, 2000.

[23] Giorgini, J.D., Benner, L.A.M., Ostro, S.J., Nolan, M.C., and Busch, M.W.: Predicting the Earth encounters of (99942) Apophis, Icarus 193, pp. 1-19, 2008.

[24] Alessi, E.M., Farrés, A., Jorba, A., Simó, C, Vieiro, A., Efficient Usage of Self Validated Integrators for Space Applications, Final Report, ESA/ESTEC contract No. 20783/07/NL/CB (2007).

[25] Standish, M.E. and Williams, J.G., Detailed description of the JPL planetary and lunar ephemerides, DE405/LE405, pp. 1–33, Electronically available as a PDF file, http://iau-comm4.jpl.nasa.gov/XSChap8.pdf.

[26] Battin, R.H.: An Introduction to the Mathematics and Methods of Astrodynamics, Second Printing. AIAA Education Series, Providence, 1987.

[27] Milani, A. and Chesley, S.R. and Chodas, P.W. and Valsecchi, G.B.: Asteroid close approaches: analysis and potential impact detection, Asteroids III, pp.89–101, 2002.

[28] Park, S. R. and Scheeres, D. J.: Nonlinear Mapping of Gaussian Statistics: theory and Applications to Spacecraft Trajectory Design, Journal of Guidance and Control, Vol. 29, No. 6, 2006.

[29] Vinogradova, T.A. Kochetova, O.M., Chernetenko, Yu.A., Shor, V.A., and Yagudina, E.I.: The Orbit of Asteroid (99942) Apophis as Determined from Optical and Radar Observations, SolarSystem Research, vol. 42, pp. 271-280, 2008.

[30] Makino, K., Berz, M.: Verified Global Optimization with Taylor Model-based Range Bounders, Transactions on Computers, Vol. 11 pp. 1611–1618, 2005.

[31] Forssell, L.S.: Flight Clearance Analysis Using Global Nonlinear Optimization Algorithms, Proc. Of the AIAA Guidance, Navigation, and Control Conferente, Austin, Texas, 2003.